Main Manuscript

Biomechanical Phenotyping Reveals Unique Mechanobiological Signatures of Early-Onset Colorectal Cancer

Nicole C. Huning[1,†], Munir H. Buhaya[2,†], Victor V. Nguyen[1,8], Afeefah Khazi-Syed[2], Haider A. Ali[1], Adil Khan[1,8], Angela Fan[2], Robert C. Fisher[2], Zhikai Chi[3], Indu Raman[4], Guangchun Chen[4], Chengsong Zhu[4], Mengxi Yu[5], Andrew R. Jamieson[5], Sara Roccabianca[6], Victor D. Varner[1,8], Cheryl M. Lewis[7], Emina H. Huang[2,7,8*], Jacopo Ferruzzi[1,8*]

[1]Department of Bioengineering
University of Texas at Dallas, Richardson, TX, USA.

[2]Department of Surgery,
University of Texas Southwestern Medical Center, Dallas, TX, USA

[3]Department of Pathology,
University of Texas Southwestern Medical Center, Dallas, TX, USA

[4]Department of Immunology,
University of Texas Southwestern Medical Center, Dallas, TX, USA

[5]Lyda Hill Department of Bioinformatics,
University of Texas Southwestern Medical Center, Dallas, TX, USA

[6]Department of Mechanical Engineering & Materials Science,
Washington University at St. Louis, St. Louis, MO

[7]Harold C. Simmons Comprehensive Cancer Center,
University of Texas Southwestern Medical Center, Dallas, TX, USA

[8]Department of Biomedical Engineering,
University of Texas Southwestern Medical Center, Dallas, TX, USA

[†]These authors contributed equally to this work

*Correspondence should be addressed to Jacopo Ferruzzi (jacopo.ferruzzi@utdallas.edu) or to Emina Huang (emina.huang@utsouthwestern.edu).

ABSTRACT

The incidence of sporadic early onset colorectal cancer (EO CRC, under 50 years of age) is rising rapidly, yet the causes behind such rise remain poorly understood. Epidemiological studies indicate that lifestyle and environmental exposures may result in chronic inflammation, which is known to trigger tissue fibrosis. We hypothesized that fibrotic remodeling and biomechanical stiffening of colorectal tissues represent hallmarks and drivers of EO CRC. Using primary human tissues, we show that EO CRC is associated with changes in collagen microstructure, increased stiffness and elevated viscosity of primary tumors. Spatial profiling and immunostaining reveal pro-fibrotic transcriptional programs in stromal cells, alongside enhanced mechanotransduction and proliferation in epithelial cells. In vitro, increased matrix stiffness promotes increased proliferation of epithelial cells in 2D and 3D colorectal cancer models. Together, these findings establish EO CRC as a disease marked by early and widespread biomechanical remodeling, suggesting that a fibrotic and stiffened tissue microenvironment may orchestrate EO CRC tumor initiation.

Keywords: colorectal cancer, early onset, average onset, biomechanics, stiffness, fibrosis

INTRODUCTION

Colorectal cancer (CRC) ranks as the third most diagnosed cancer worldwide and the second leading cause of cancer-related death in the United States (*1–3*). Over the past decades, increased rates of routine colonoscopy screening have led to a steady decline in the incidence of average-onset colorectal cancer (AO CRC), which affects patients at or above 50 years of age (*4*). In contrast, early onset colorectal cancer (EO CRC), which affects patients under 50 years of age (*5*), has been rising by 0.5% to 2.4% annually for three decades, comprising 12% of all CRCs diagnosed in the United States since 2020 (*6*). Based on current estimates, the most rapid increase in EO CRC will be experienced by individuals between 20 and 34 years old (*7*). Younger patients are also more likely to present advanced-stage disease (*8*). If the current trend persists, EO CRC is expected to increase by 124% by the year 2030 (*9*). In response, independent panels of experts now recommend starting colonoscopy screening at age 45 instead of 50 (*10*, *11*). However, these updates in medical guidelines were made in the absence of a clear mechanistic understanding of EO CRC pathogenesis or progression. Thereby, critical gaps in knowledge persist and hinder the development of tailored screening tools and treatments strategies for younger patients.

EO CRC has no unique mutational drivers differentiating it from AO CRC (*12–14*). The rapid rise in incidence over just three decades suggests that genetic changes alone are insufficient to explain the emergence of this disease (*15*). Pathologically, EO CRC often presents at a late stage at diagnosis with aggressive features including mucinous, signet ring, and poorly differentiated tumors (*12*). Further, the majority of EO CRCs are microsatellite stable (MSS) and sporadic in nature (i.e., cannot be attributed to genetic germline mutations) (*16*). Anatomically, EO CRC is often located within the distal colon or rectum, a feature referred to as left-sidedness that is more pronounced than in AO CRC, which occurs more frequently in the proximal colon (*12*, *17*). The

birth-cohort effect hypothesis (*18*) suggests that early life exposures are critical to understanding the etiology of EO CRC, with adults born in the 1990s having a higher risk of developing both colon and rectal cancers than adults born in the 1950s (*19*). Emerging evidence supports consideration of chronic, low-grade inflammation as a key contributor to EO CRC initiation (*5*, *18*, *20*), which aligns with the well-established link between inflammation and oncogenesis (*21–23*). In the context of EO CRC, it is conceivable that both lifestyle exposures and the birth-cohort effect are permissive of chronic inflammation. In turn, chronic inflammation may also promote dysbiosis and microbiome alterations, further contributing to disease development (*9*, *24*).

A key downstream consequence of chronic inflammation is activation of tissue-resident fibroblasts and remodeling of the extracellular matrix (ECM), leading to deposition and reorganization of a collagen-rich ECM. Therefore, chronic inflammation leads to changes in biomechanical function through fibrotic remodeling (*25–28*). This process, known as *desmoplasia*, results in the chronic deposition and remodeling of collagenous tissue. Desmoplastic remodeling of the tumor microenvironment has been shown to drive malignant phenotypes in other solid tumors such as breast (*29*) and pancreatic (*30*) cancers. However, the role of desmoplasia in CRC is less clear, with studies indicating a similar pathogenic role (*31*, *32*) and other reports suggesting a protective role (*33*, *34*). Prior studies have reported altered tissue stiffness in AO CRC (*35–38*), though biomechanical data on EO CRC are still missing.

To fill this gap in knowledge, we quantified the biomechanical properties of primary tumors and matched normal tissues from AO and EO CRC patients. We hypothesized that, as a result of chronic inflammation, tissues from EO CRC patients are more fibrotic and thus become biomechanically stiffer. Our results consistently reveal that collagen remodeling and mechanical stiffening are elevated in EO CRC tissues compared to AO CRC, with structural and mechanical

abnormalities occurring also in histologically normal tissues from EO CRC patients. Furthermore, we show that these changes in connective tissue structure and mechanics trigger altered mechanotransduction and increased proliferation in colonic epithelial cells. Our findings suggest that biomechanical stiffening may serve as both a driver and diagnostic predictor of EO CRC. Overall, we identify increased tissue stiffness as a quantifiable hallmark of EO CRC, which could serve as a potential biomarker to stratify cancer risk in young populations.

RESULTS

EO CRC shows preferential distal localization compared to AO CRC

To investigate the structural and biomechanical properties of EO CRC, we collected colonic tissue specimens harvested from patients undergoing surgical resection. Our study cohort included 19 patients with AO CRC (68 ± 11 years of age) and 14 patients with EO CRC (44 ± 2 years of age) with demographic information and clinical characteristics listed, respectively, in Tables S1 and S2. Both groups included men and women of mixed ethnicities and races (Tables S1 and S2). Given prior reports implicating obesity in EO CRC risk (*5*, *9*, *20*, *39*), we compared the body mass index (BMI) between cohorts. We found that the mean BMI for AO CRC patients was 32 (class I obesity), whereas EO CRC patients had a lower mean BMI of 27.2 (overweight range). While both groups fall within elevated BMI categories, the lack of a statistically significant difference in our cohort suggests that obesity may not be a defining feature in EO CRC, aligning with prior observations that EO CRC occurs across the BMI spectrum (*40*). Consistent with patients who present for curative resection, tumor stage distribution was similar between groups, with most patients having stage II or III CRC. The most striking difference between cohorts was tumor location (Fig. S1). In our cohort, the most frequent location for AO CRC was the cecum (36.8%) and the least frequent location was the rectum (0%). Conversely, the most frequent

location for EO CRC was the sigmoid colon (42.9%) and the least frequent location was the right colon along with the hepatic and splenic flexures (0%). Despite potential selection bias in our small patient cohort, our data are consistent with large epidemiological studies (*12*) showing that EO CRC more frequently localizes to the left colon and rectum compared to AO CRC (Fig. 1A, Fig. S1).

EO CRC tissues exhibit elevated material stiffness and viscosity

For each patient, we collected primary tumor tissues as well as matched normal tissues (retrieved at least 5 cm from the tumor) and extracted cylindrical tissue plugs (3 mm in diameter) using a biopsy punch for *ex vivo* biomechanical testing (Fig. 1B). We quantified the mechanical properties of such tissue plugs using a computer-controlled system which estimates tissue-generated forces by measuring the deflection of an elastic cantilever beam (Fig. 1C). Tissue stiffness was assessed at two distinct length scales via mesoscale (tens of micrometers) and macroscale (millimeter range) measurements, requiring distinct modeling approaches. For mesoscale properties, a cylindrical indenter having a radius of 38.1 μm (Fig. 1D) was used to conduct local force-indentation tests (Fig. 1E) and to estimate the local Young's modulus under the assumption of linear elastic behavior (Fig. 1F). We modified previous protocols (*41*, *42*) and used the cylindrical indenter to impose quasi-static small deformations (up to 5% of the total height for each tissue plug) and measure the resulting elastic forces generated on the mucosal surface (Fig. S2A-H). At this length scale, both cancer and matched normal tissues from EO CRC are materially stiffer than their AO counterparts (Fig. 1F). Within each patient cohort, cancer and matched normal tissues showed no statistically significant differences in stiffness, although cancer tissues revealed a broader distribution of tissue stiffness than matched normal tissues (Fig. S2I-J), consistent with other reports (*36*, *43*).

To validate these mesoscale findings, we assessed macroscale tissue properties by pairing the cantilever beam with a 6mm × 6mm square platen (Fig. 1G). Following our previous work (*44*, *45*), we performed stress relaxation tests in unconfined compression (Fig. 1H) and used the steady-state stress values to estimate the global Young's modulus (Fig. 1I). We employed this method to impose large deformations (up to 20% of the total height for each tissue plug) and measure the resulting viscoelastic forces generated by the tissues while recording the radial tissue expansion due to the Poisson effect (Fig. S3A-G). These combined measurements allowed us to estimate the stress developed within each tissue upon compression (Fig. S3H). Interestingly, by combining the neo-Hookean shear moduli and the Poisson's ratios measured from each specimen, we calculated Young's moduli that are comparable to those obtained using local indentation (Fig. 1I), thereby validating our local measurements.

In addition to increased stiffness, EO tissues also exhibited increased viscosity (Fig. 1J and Fig. S3I-K). In fact, stress relaxation data were modeled using a nonlinear Maxwell-Wiechert model (Fig. S4A-B), appropriately modified from previous reports (*46*, *47*) to capture colorectal tissue viscoelasticity. Using such model, we found that both matched normal and cancer tissues from EO CRC are more viscous than AO CRC tissues (Fig. 1J). Indeed, human colorectal tissues displayed a mild but noticeable nonlinearity which could be modeled by incorporating a nonlinear spring in parallel to two Maxwell elements (Fig. S4C-D). Quantification of individual model parameters revealed that the nonlinear spring parameters (c_a, c_b) are not significantly different between AO and EO CRC (Fig. S4E-F). Instead, we found that the coefficient of viscosity for the fast Maxwell element (η_1) was higher in both matched normal and cancerous EO tissues (Fig. 1J) while the slow Maxwell element (η_2) and the Maxell spring constant (c_m) are consistently elevated only in EO matched normal tissues (Fig. S4G-I). Taken together, our multiscale

biomechanical data interpreted using both linear elastic and nonlinear viscoelastic modeling reveal that human tissues from EO CRC are materially stiffer and more viscous than human tissues from AO CRC.

EO CRC displays consistent patterns of fibrotic collagen remodeling

To investigate the structural basis of the observed changes in tissue mechanics, we examined histological cross-sections from formalin-fixed and paraffin-embedded (FFPE) tissues to quantify changes in collagen fiber content, distribution, and organization. Masson's Trichrome staining was used to differentiate collagen (blue) from cellular elements (red) and a colorimetric image-based quantification was performed to determine collagen and cytoplasm area fractions (Fig. 2A, Fig. S5A-E). Matched normal tissues preserved a well-organized structure comprising mucosa, submucosa, muscularis propria, and serosa. Accordingly, collagen content was higher in the normal submucosa with respect to the normal mucosa (Fig. S5F-G). Conversely, cancer tissues lost such layered organization and displayed interspersed stromal and epithelial compartments. When comparing collagen content between the normal submucosa and the cancer stroma in AO and EO CRC tissues, we found that both AO and EO cancer tissues exhibit a lower collagen content with respect to the normal submucosa, which likely reflects an increased tumor cellularity (Fig. 2B-C). However, EO cancers retained more collagen than AO cancers, suggesting enhanced matrix deposition and remodeling in EO CRC (Fig. 2C).

To assess collagen fiber structure, we performed Picrosirius Red (PSR) staining in combination with polarized light (POL) imaging (Fig. 2D). This approach distinguishes collagen fiber thickness, packing, and maturity based on the color of birefringent fibers: red denotes thicker, tightly packed, and mature fibers; orange-yellow represent intermediate thickness and packing; green indicates thinner, loosely packed, and immature fibers (*48–51*) (Fig. S6). EO tissues, both

cancer and matched normal, contained higher proportions of thick (red) collagen fibers compared to AO tissues (Fig. 2E-F), which mirrors the increased tissue stiffness observed biomechanically (Figs. 1F and 1I). While PSR staining is widely used to assess fibrosis, it lacks subtype specificity and POL imaging is dependent on the orientation of the collagen fiber bundles (*52*). To address the latter concern, we quantified the architectural organization of stromal collagen using multiphoton label-free Second Harmonic Generation (SHG) imaging (*53–56*) from Hematoxylin and Eosin (H&E) stained slides (Fig. 2G). SHG images were analyzed using ridge detection (*57*) to quantify mean fiber length, width, orientation, and SHG signal intensity across all pixels (Fig. S7A-C). Compared to AO normal tissues, EO matched normal tissues exhibited shorter collagen fibers with an elevated SHG signal intensity, reflecting increased density of collagen fibers. SHG signal intensity decreased in tumors relative to matched normal tissues in both cohorts paralleling a reduction in collagen fiber width (Fig. S7D-E). Notably, we found that EO CRC collagen fibers are longer and more aligned with respect to fibers in EO normal or AO cancer samples (Fig. 2H-I and S7F-G), a pattern reminiscent of the aligned collagen found in invasive breast cancers (*58*). This finding is particularly relevant as it may link collagen alignment with the highly invasive and metastatic behavior reported in EO CRC (*9*).

These data demonstrate that EO CRC exhibits consistent fibrotic features with denser and more aligned collagen fibers – across both tumor and adjacent normal tissues. These structural alterations support the increased tissue stiffness observed in EO CRC and point to fibrosis as a defining feature of the EO CRC tumor microenvironment.

EO CRC presents unique cell morphologies and epithelial-mesenchymal phenotypes

To explore the cellular characteristics underlying a dysregulated ECM in EO CRC, we performed high-resolution immunofluorescence imaging on a subset of tissue samples stained with

PanCK, an epithelial marker; Vimentin, a mesenchymal marker; and CD45, an immune marker (Fig. 3A). Although CD45 successfully labeled immune cells, the minimal immune infiltration resulted in low signal intensity, leading to its exclusion from downstream quantifications. Matched normal tissues maintain spatially distinct epithelial and mesenchymal compartments, whereas cancer tissues display a disorganized pattern of epithelial cell clusters surrounded by mesenchymal cells (Fig 3B). We conducted single-cell segmentation using an established deep-learning algorithm (*59*), enabling quantification of 2,155,046 cells from 11 patient-derived samples across the four groups (Fig. S8). For each segmented cell, we extracted features including morphology (cell area and aspect ratio) and marker expression (PanCK and Vimentin intensity) (Fig. 3C). Across all samples, EO tissues exhibited consistent morphological distinctions. The cell area was smaller in both normal and tumor tissues from EO CRC compared to AO CRC, although cancer cells were larger than matched normal cells within each group (Fig. 3D). The cell aspect ratio showed greater variability: EO normal tissues have higher aspect ratios (i.e., are more elongated) while EO cancer have lower aspect ratios (i.e., are more rounded) compared to their corresponding AO counterparts (Fig. 3E). After segmentation, the fluorescence intensity of the PanCK (epithelial) and Vimentin (mesenchymal) markers was z-normalized to facilitate comparisons of cellular identity markers across groups. We found that PanCK expression is lower in EO than in AO across both normal and tumor tissues (Fig. 3F). In contrast, Vimentin expression follows the opposite pattern: EO cells display higher Vimentin levels than AO cells, despite cancer tissues generally express lower Vimentin than matched normal tissues (Fig. 3G).

To further characterize the observed cellular heterogeneity, we applied unsupervised Louvain clustering (*60*) which identified four dominant cell clusters based on the average cell morphology and marker expression: epithelial-large (PanCK-high, Vimentin-low, cell area-high),

epithelial-small (PanCK-high, Vimentin-low, cell area-low), stroma (PanCK-low, Vimentin-high, cell area-high), and immune (PanCK-low, Vimentin-high, cell area-low) (Fig. S9). This classification yielded spatial distributions that reflected qualitatively the cellular patterns observed in raw immunofluorescence images (Fig. S9). Reanalysis of the cellular morphology and marker expression results by cluster confirmed that both EO normal and cancer cells display consistently smaller areas across all phenotypes (Fig. S10). This result potentially reflects the elevated compressive stress experienced by all cell types within the tumor microenvironment (*61–63*). Stromal cells in EO tissues showed a consistent increase in aspect ratio (Fig. S10), mirroring the increased collagen fiber alignment observed in EO cancers (Fig. 2I). This finding suggests that fibroblast-like mesenchymal cells actively polarize and align the tumor ECM in EO CRC. Regarding marker expression, both epithelial-large and epithelial-small cells in EO CRC co-express higher levels of PanCK and Vimentin (Fig. S10), which indicates a mixed epithelial-mesenchymal phenotype. Overall, our single-cell morphological analysis demonstrates that EO CRC exhibits altered cellular morphologies (smaller areas amongst all cells, elongated stromal cells) and increased epithelial-mesenchymal characteristics compared to AO CRC.

Mesenchymal cells in EO CRC present pro-fibrotic transcriptional signatures

Mesenchymal cells, particularly cancer-associated fibroblasts (CAFs), play a critical role in sculpting the tumor microenvironment and in promoting cancer progression (*64–66*). Given the increased tissue stiffness, collagen remodeling, and stromal alignment in EO CRC, we next examined spatially-resolved RNA expression in FFPE tissue samples from AO and EO CRC patients using the GeoMx® RNA platform (*67*, *68*). We first focused on 13 Vimentin-positive regions of interest (ROIs) from matched normal samples (6 ROIs from AO tissues and 7 ROIs from EO tissues) and 40 Vimentin-positive ROIs from cancer samples (17 ROIs from AO tissues

and 23 ROIs from EO tissues) for spatial transcriptomic analysis (Fig. 4A). Differential expression analysis between EO cancer and AO cancer revealed 32 differentially expressed genes (DEGs, adjusted p-value < 0.05, |log2 Fold Change| > 1) in stromal cells, with 30 genes upregulated and only 2 genes downregulated in EO cancer (Fig. S11). Gene ontology (GO) analysis revealed significant enrichment of pathways involved in ECM organization, collagen metabolism, and angiogenesis in EO cancer (Fig. 4B). Based on this evidence, we conducted a Gene Set Enrichment Analysis (GSEA) using a curated intestinal fibrosis gene set (*69*). In accordance with our biomechanical and histological findings, we discovered that a transcriptional program promoting intestinal fibrosis is active in EO CRC (Fig. 4C). We next examined key genes within fibrosis-related pathways across normal and cancer samples in both age groups (Fig. 4D-F). First, we examined genes involved in collagen fibrillogenesis and found a significant increase in the expression of genes associated with collagens type I and III (*COL1A1*, *COL1A2*, and *COL3A1*) in cancer tissues with respect to normal for both age groups, while we found no differences between EO and AO cancers (Fig. S12A). In contrast, expression of collagen type VI (*COL6A1* and *COL6A2*) was significantly upregulated in EO cancer along with the expression of decorin (*DCN*), a small proteoglycan which regulates collagen fiber organization (Fig. 4E). Next, we investigated genes involved in ECM remodeling, and found that EO cancers upregulate genes associated with matrix crosslinking, such as lysyl oxidase-like 1 (*LOXL1*) and tissue transglutaminase (*TGM2*), while matrix degradation genes, such as matrix metalloproteinases (*MMP2*, *MMP9*, and *MMP12*) demonstrated only modest differences in expression (Fig. S12B). Instead, the gene encoding tissue inhibitor of metalloproteinases 1 (*TIMP1*) was significantly upregulated in EO cancer, suggesting a shift in the proteolytic balance toward ECM accumulation (Fig. 4D). We also observed elevated expression of genes involved in cell-matrix adhesion and signaling, such as thrombospondin 1

(*THBS1*), the integrin subunit α5 (*ITGA5*), and *CD44* (Fig. S12C) in EO cancers. Lastly, genes involved in inflammation and angiogenesis, such as the C-X-C motif chemokine ligand 1 (*CXCL1*), the monocyte chemoattractant protein-1 (MCP-1 or *CCL2*), and the platelet-derived growth factor receptor beta (*PDGFRβ*), were upregulated in EO cancer with respect to AO cancer (Figs. 4F and S12D-E). Our trascriptional analysis of Vimentin-positive cells confirms that stromal cells in EO CRC exhibit a distinct pro-fibrotic transcriptional program, characterized by enhanced collagen deposition, cross-linking, adhesion signaling, and inflammatory remodeling. These features likely contribute to the fibrotic and mechanically altered tumor microenvironment that distinguishes EO CRC from AO CRC.

Epithelial cells in EO CRC exhibit enhanced proliferation and altered mechanosensing

The second step in our digital spatial profiling was to focus on epithelial cells by identifying PanCK-positive ROIs from cancer samples (9 ROIs from AO tissues and 10 ROIs from EO tissues) for spatial transcriptomic analysis (Fig. 5A). Differential expression analysis identified 769 differentially expressed genes (DEGs) in epithelial cells in EO relative to AO cancer, with 421 genes upregulated and 348 genes downregulated in EO cancer (adjusted p-value < 0.05, $|\log2 \text{ Fold Change}| > 1$, Fig. 5B). Upregulation of genes encoding olfactomedin 4 (*OLFM4*) and mutiple histone proteins and variants (*H1.5*, *H2BC9*, *H2BC10*, *H3C3*, *H3C7*, *H3C8*) indicates enhanced cell proliferation in EO CRC (Fig. 5B). In addition, upregulation of the neuronal pentraxin 2 (*NPTX2*) gene has been associated with proliferation, epithelial-to-mesenchymal transtion, and metastasis in CRC (*70*). To contextualize these findings, we assessed expression patterns associated with the consensus molecular subtype (CMS) classification of CRC (*71*, *72*). By focusing on the two intrinsic subtypes iCMS2 and iCMS3 (*72*) in our patient cohort, unsupervised hierarchical clustering revealed the expected dichotomy between these subtypes, with iCMS2

samples showing elevated expression of WNT/β-catenin and MYC signaling, while iCMS3 samples showed upregulation of MAPK pathway genes and inflammatory response signatures (Fig. S13). Yet, the EO and AO cancer samples did not segregate into these two distinct subtypes (Fig. S13). This finding further supports that AO and EO CRC may not be distinguished based on intrinsic epithelial features but rather based on microenvironmental factors.

Gene ontology (GO) analysis of epithelial cells from EO cancer compared to AO cancer revealed enrichment of pathways related to cell division, mitotic processes, and metabolism (Fig 5C). Notably, the stem cell marker *OLFM4* is highly upregulated in EO CRC while another stem cell marker *LGR5* is highly downregulated in EO CRC (Fig. S14), mirroring trends observed in intestinal stem cells cultured on substrates of increasing stiffness (*73*). To confirm the observed trends in transcriptional data based on a limited number of epithelial ROIs, we conducted immunohistochemistry staining of tissue samples using the cell proliferation marker Ki67 and found evidence of increased cell proliferation in both EO matched normal and EO cancer samples (Fig 5D). We noted that epithelial cells in EO CRC reveal a distinct pattern of increased proliferation which mirrors the observed trends in tissue stiffness (cf., Fig. 1). These data support the hypothesis that epithelial proliferation may be mechanically regulated in EO CRC.

We next analyzed mechanotransductive signaling using eight major mechanotransduction categories. We found that genes related to mechanosensitive transcription factors (Mechano TFs), mechanosensors, cytoskeletal components, canonical Hippo pathway, and Rho signaling were unexpectedly downregulated in EO CRC (Fig. 5E). Conversely, genes involved with focal adhesion complexes, integrins, and the linker of nucleoskeleton and cytoskeleton (LINC) complex demonstrated upregulation in EO CRC (Fig. 5E), suggesting a complex set of alterations in the epithelial mechanosensing machinery. The selected mechanotransduction pathways did not reach

statistical significance at an adjusted p-value of 0.05 (Fig. 5E). However, individual mechanotransduction genes within these pathways exhibited substantial expression changes (Fig. S15, |log2 Fold Change| > 1). Given the established role of the Hippo pathway in regulating the proliferation of intestinal epithelial cells (*74*), we were surprised to find downregulation of *YAP1* (YAP) and *WWTR1* (TAZ), along with elevated expression of *LATS1* (Fig. S16A). Furthermore, the TEA-domain (TEAD) transcription factors *TEAD1-4* displayed a mixed pattern of expression (Fig. S16B), while genes downstream of the Hippo pathway were upregulated (Fig. S16C). This findings suggested that, while the canonical Hippo pathway is downregulated in EO CRC, the mechanosensitive effectors YAP/TAZ might be active in epithelial cells and partially responsible for the observed pattern of increased cell proliferation. To reconcile this apparent contradiction, we examined active (non-phosphorylated) YAP in tissue samples via immunofluorescence. We found evidence of increased nuclear YAP activity in epithelial cells from both EO matched normal and EO cancer samples with respect to their AO counterparts (Fig. 5F). This finding indicates elevated YAP activity in EO CRC despite downregulated canonical Hippo signaling, which suggests that YAP may be activated through Hippo-independent mechanisms, such as integrin-mediated mechanotranscduction. We conducted a GSEA using a validated YAP transcriptional signature (*75*) and confirmed upregulation of YAP activity in EO CRC epithelial cells (Fig. 5G). The contradictory findings from spatial transcriptomics (downregulated Hippo signaling) and immunofluorescence (active YAP in cell nuclei) of EO CRC epithelial cells may be explained by the fact that integrins, focal adhesions, and the LINC complex can activate YAP in response to fibrotic tissue stiffening independently from activation of the Hippo pathway (*76*). In response to YAP activation, negative feedback in the regulatory gene network may be triggered and affect the expression of the Hippo pathway genes, resulting in the observed downregulation of the canonical

Hippo pathway (Fig. S16). Taken together, these data support a model in which fibrotic remodeling in EO CRC directly contributes to epithelial activation and proliferation via YAP-mediated mechanotransduction.

Microenvironmental stiffness enhances epithelial proliferation

To isolate the contribution of mechanical cues to epithelial cell proliferation, independent of other *in vivo* factors, we employed both two-dimensional (2D) and three-dimensional (3D) *in vitro* models. First, we utilized CRC cell lines cultured on polyacrylamide (PA) substrates of graded stiffness (*77–79*) to investigate mechanobiological regulation of CRC cell proliferation. Based on the material stiffness values measured from primary patient samples (Figs. 1F and 1I), we restricted our analysis to relatively moderate substrate stiffnesses (Soft = 0.2-0.8 kPa and Stiff = 3.2-4.4 kPa, as confirmed via unconfined compression and shown in Fig. 6) compared to other studies (*73*, *80*, *81*). The colon cancer cell lines HT29 (44-year-old patient, used here as a model of EO CRC) and SW480 (50-year-old patient, used here as a model of AO CRC) were seeded on collagen- and Matrigel-coated PA gels of graded stiffness (Fig. S17) for 72 hours (Fig. S17A-B). We measured the cellular aspect ratio and the percentage of EdU-positive cells and found that SW480 cells show greater mechanoresponsiveness than HT29 cells, both in terms of morphology and proliferation (Fig. S17C-D). Importantly, when PA gels are coated with collagen, which reproduces the stromal environment, SW480 cells are highly proliferative and elongated regardless of substrate stiffness (Fig. S17D). Conversely, when PA gels are coated with Matrigel, which reproduces the native basement membrane, SW480 cells exhibit changes in morphology and proliferation as a function of increasing substrate stiffness (Fig. S17D). We found that, over multiple biological replicates, HT29 cells display modest changes in aspect ratio and EdU incorporation with increasing stiffness, with significant changes in morphology and proliferation

only on glass (Fig. 6A-D). Instead, SW480 cells exhibited a more elongated morphology and increased proliferation with increasing stiffness, as indicated by higher aspect ratios and EdU incorporation on both stiff gels and glass (Fig. 6E-H). Therefore, despite differences in mechanosensitive responsiveness across ECM coatings and cell types, elevated substrate stiffness promoted cancer cell proliferation in both models of EO CRC (HT29) and AO CRC (SW480).

To assess the role of 3D mechanosensitivity using clinically relevant models, we derived CRC organoids from a subset of patients within our patient cohort (Tables S1 and S2), using established methods (*82*, *83*). Organoids from unique AO and EO CRC patients (Table S3) were cultured in hyaluronic acid-tyramine (HA-Tyr) hydrogels of different concentrations (2.5 mg/mL and 8 mg/mL), which corresponded to different stiffness values (Fig. 6I). After 7 days of culture, organoids in stiff hydrogels exhibited larger sizes regardless of the tissue of origin (AO vs. EO) (Fig. 6J). These changes in organoid morphology are accompanied by changes in cell proliferation (Fig. 6K). These *in vitro* findings demonstrate that increased microenvironmental stiffness may facilitate epithelial proliferation, independent of the underlying mutational status or age of the tumor of origin. These results support our *ex vivo* observations and suggest that microenvironmental stiffening may directly contribute to epithelial activation and facilitate tumor progression in fibrotic EO CRC.

DISCUSSION

The etiology of the recent rise in incidence and mortality of EO CRC remains poorly understood (*5*, *9*). Since most cases of sporadic EO CRC are multifactorial, involving both environmental and lifestyle factors (*18*), there is a pressing need to uncover mechanistic insights and to identify predictive biomarkers capable of stratifying patients at high risk for metastatic disease and recurrence, particularly among stage II and III patients. In this study, we identify tissue

stiffening and fibrotic remodeling as consistent biophysically measurable hallmarks of EO CRC. Furthermore, we link these mechanical changes to collagen remodeling in the colonic stroma and to mechanobiological changes in the colonic epithelium (Fig. 7).

Building on evidence that chronic, low-grade inflammation underlies EO CRC initiation (*5*, *18*, *20*), we hypothesized that fibrosis and mechanical stiffening of colorectal tissues may serve both as early and active drivers of EO CRC progression. Based on this premise, the first objective of this study was to compare tissue biomechanics between EO CRC and AO CRC patient samples. While several reports have examined altered tissue mechanics in primary (*35–38*, *43*) and metastatic (*84*, *85*) CRC, most relied on atomic force microscopy (AFM) which probes tissue stiffness at nano- and microscale resolution but requires sample processing steps including adhesive mounting (*43*), dehydration (*36*), and cryo-sectioning (*37*, *38*, *84*, *85*) that may alter the native tissue mechanics. Additionally, AFM captures localized mechanical properties of cell and ECM structures rather than the broader tissue-level mechanical properties relevant for diagnostic and therapeutic applications. For these reasons, here we used mesoscale indentation (*86*) and macroscale compression (*45*), both of which require minimal tissue preparation and enable evaluation of bulk mechanical behavior. Our multi-scale mechanical measurements of primary CRC tissues yielded stiffness values under 3kPA, which represents an average of the heterogeneous mechanical landscape that AFM resolves at higher resolution, including soft cellular regions (<1 kPa) and stiffer ECM-rich structures (~10-20 kPa). Differences between normal and cancer tissues were more modest than previously reported (*35*, *43*, *37*) possibly due to patient heterogeneity or differences in testing methodology. Notably, both mesoscale and macroscale approaches revealed significantly elevated stiffness in EO CRC tissues relative to AO CRC (Fig. 1).

While tissue stiffness – quantified as the Young's elastic modulus – can be extracted from both mesoscale indentation and macroscale compression approaches under the assumption of linear elastic behavior, characterizing nonlinear elastic properties and viscoelastic behavior requires large deformations and time-resolved measurements, respectively. To quantify the nonlinear viscoelastic properties of CRC tissues, we adopted stress-relaxation testing in macroscale compression paired with a nonlinear Maxwell-Wiechert model (*46*, *47*). Our data reveal increased tissue viscosity as an additional biophysical signature of EO CRC (Figs. 1 and S4), a distinct biomechanical feature not previously reported. Given the emerging recognition of matrix viscoelasticity as a critical regulator of cellular and tissue dynamics (*87*, *88*), we propose that this observed increase in viscosity in EO CRC represents an important mechanobiological characteristic that warrants further investigation.

Strikingly, we found that not only cancerous tissues but also normal tissues from EO patients exhibited elevated stiffness and viscosity compared to tissues from AO patients (Fig. 1), suggesting that mechanical remodeling may precede malignant transformation and may contribute to the development of EO CRC. Indeed, quantitative PSR staining and POL imaging revealed that EO normal tissues are enriched with red (thicker, most tightly packed and mature) collagen fibers, while they display reduced orange and yellow (intermediate thickness and packing) collagen fibers, with minimal green (thinnest, loosely packed and less mature) collagen fibers (Figs. 2 and S6). By examining the microstructural organization of collagen via multiphoton SHG imaging, we found that EO normal tissues are characterized by an increased SHG intensity, a reduced fiber length, and similar fiber width and orientation with respect to AO normal tissues (Fig. S7). Collectively, these results reveal that normal tissues from EO patients contain shorter, denser, and therefore more tightly packed collagen fibers which are likely responsible for the observed increase

in the stiffness of matched normal tissues. In turn, structural and mechanical differences between AO and EO normal tissues raised the possibility that fibrotic remodeling and tissue stiffening may represent microenvironmental cues that predispose malignant transformation of a normal epithelium in EO CRC.

To investigate the structural causes of altered tissue mechanics in cancer samples, we combined quantitative histological and immunofluorescence analyses (Figs. 2 and 3). EO cancer tissues exhibited thinner, longer, and more aligned fibers compared to AO cancer tissues (Figs. S5-S7). At the same time, EO cancer tissue exhibited elongated stromal cells and an overall increase in the expression of the mesenchymal marker Vimentin (Figs. S8-S10). As for the ECM, the architectural remodeling of collagen in EO cancer resembles the radially aligned tumor-associated collagen signatures (TACS) observed in breast cancer (*89*), which correlate with increased invasiveness and poor prognosis (*58*). This parallel suggests that collagen alignment by stromal cells may provide a biophysical mechanism to explain the aggressive invasive behavior characteristic of EO CRC.

Since collagen remodeling in the stroma is primarily driven by CAFs, and fibroblast activation protein (FAP)-positive CAFs are enriched at the invasive margin of human EO CRC tissues (*90*), we used spatial transcriptomic analysis to explore the transcriptional programs of Vimentin-positive stromal cells (Fig. 3). While canonical CAF markers (*ACTA2*, *FAP*, *PDGFA*, *PDGFB*) were not selectively enriched, we observed upregulation in ECM remodeling genes in EO CRC. The most significantly upregulated genes are associated with ECM crosslinking (*LOXL1/2*, *TGM2*), MMP inhibition (*TIMP1*), and increased cell-ECM interactions (*THBS1*, *ITGA5*, *CD44*), thereby supporting the accumulation of a stiffer and more aligned ECM in EO CRC (Figs. 4 and S12). In parallel, elevated expression of pro-inflammatory mediators (*CXCL1*,

CCL2) and immunomodulatory ECM proteins (*COL6A1*) support the presence of a pro-inflammatory, immune-recruiting stromal environment (*91*). In PanCK-positive epithelial cells, spatial transcriptomics revealed upregulation of genes involved in cell proliferation and metabolism in EO CRC (Fig. 5A-D). Among genes involved in cell proliferation, the stem cell marker *OLFM4* was significantly upregulated while another stem cell marker *LGR5* was significantly downregulated in EO CRC. Notably, the same pattern in stem cell marker expression was independently observed in intestinal stem cells cultured on substrates of increasing stiffness (*73*). At the same time, it has been shown that LGR5-negative colon cancer stem cells are characterized by lower stiffness and increased motility than their LGR5-positive counterparts (*81*). Together, these findings suggest that epithelial cells in EO CRC may be more responsive to mechanical cues from the local tissue microenvironment.

We found that this responsiveness is mediated, at least in part, by enhanced nuclear YAP activity. Despite canonical Hippo signaling being transcriptionally downregulated in EO CRC (Figs. 5E and S16), immunofluorescence revealed increased nuclear localization of active YAP protein in both matched normal and cancerous EO epithelia (Fig. 5F). GSEA confirmed coordinated upregulation of YAP target genes in EO CRC relative to AO CRC, reconciling the seemingly contradictory findings of downregulated Hippo pathway components with increased YAP activity. This suggests that enhanced YAP activity in EO CRC epithelial cells likely results from post-transcriptional protein stabilization through integrin signaling and focal adhesion dynamics, rather than regulation through the canonical Hippo pathway. Indeed, YAP activity can be directly triggered by mechanical forces that deform the nucleus, potentially involving the LINC complex (*92*, *93*), as suggested by our data.

To directly test the effect of matrix stiffness on epithelial cell proliferation, we examined stiffness-dependent changes in cell morphology and proliferation using CRC cells cultured on 2D and in 3D hydrogels (Fig. 6). In 2D experiments using CRC cell lines cultured on PA hydrogels, SW480 cells (a model of AO CRC) were more mechanosensitive than HT29 cells (a model of EO CRC), exhibiting increased elongation and proliferation on stiffer substrates. While differences in mechanobiological responses between different cell lines are to be expected, we found that the observed mechanosensitive changes depend on the type of ECM used to functionalize PA substrates. In fact, stiffness-dependent changes emerged only on Matrigel-coated substrates, while both cell morphology and proliferation of cells cultured on collagen I-coated substrates were consistently elevated regardless of substrate stiffness (Fig. S17). Coating substrates with Matrigel better recapitulates the basement membrane environment of colonic epithelial cells than collagen I coating and therefore is more relevant as a model of CRC initiation. Importantly, we focused our *in vitro* analysis on a moderate stiffness range (0.2-to-4.4 kPa) that reflects mechanical properties measured in primary EO CRC tissue samples (Fig. 1), with the goal of reproducing the mechanobiological responses of epithelial cells in EO CRC. Within this stiffness range, our findings emphasize that both ECM composition and stiffness influence epithelial mechanobiology. The impact of microenvironmental stiffness on cancer cell proliferation was further validated using 3D primary organoids cultured in hydrogels of tunable stiffness (Fig. 6I-K), where proliferation was dictated by hydrogel stiffness rather than by the tissue of origin (AO vs. EO CRC). In fact, organoids cultured for 7 days in soft hydrogels were consistently less proliferative while organoids cultured for the same period in stiff hydrogels were consistently more proliferative. The key observation here is that the differences in epithelial cell proliferation observed *ex vivo* (Fig. 5)

disappear by culturing epithelial organoids *in vitro* and can be reproduced by tuning solely the mechanical properties of the tumor microenvironment.

The primary limitation of this study is the relatively small sample size, comprising 19 AO CRC and 14 EO CRC tissue pairs (each containing matched normal and cancer samples). Additionally, some patients did not yield complete biomechanical datasets due to insufficient tissue size or damage during preparation and testing. Our sample set also had a notable absence of rectal cancers in the AO CRC group, likely reflecting more aggressive chemoradiation therapy that reduces tumor size and requires prioritizing tissue for essential clinicopathological analyses over research use. Furthermore, spatial transcriptomic analysis was performed on a limited number of ROIs and was not consistently conducted on both matched normal and cancer tissues within PanCK-positive ROIs. Despite these constraints, a coherent mechanobiological framework emerges from our multi-scale approach integrating biomechanical measurements, quantitative histology, cellular phenotype analysis, spatial transcriptomics, and *in vitro* modeling. This work therefore represents the first comprehensive mechanobiological characterization of EO CRC. We demonstrate that pro-inflammatory and pro-fibrotic remodeling drives tissue stiffening, leading to enhanced epithelial YAP activity and proliferation. We propose that these mechanobiological signatures play a key role in promoting EO CRC development and progression (Fig. 7).

Future investigations should focus on three key areas: (1) elucidating the biochemical and biomechanical crosstalk between stromal and epithelial cells during EO CRC initiation and progression, (2) systematically modulating both microenvironmental stiffness and viscosity to define their respective contributions to EO CRC pathogenesis, and (3) evaluating compositional and mechanical biomarkers as early predictors of EO CRC progression for improved diagnostic and therapeutic strategies.

MATERIALS AND METHODS

Patients. Tissue specimens were obtained from patients who underwent operative resection for colorectal cancer at either the Cleveland Clinic (IRB 13-1159) or at the University of Texas Southwestern Medical Center (IRB 2021-0161). The inclusion criteria were as follows: individuals with age above 18 years, decisionally competent, non-pregnant, non-incarcerated, with colorectal cancer undergoing exploration with resection of bowel. Patient demographics, stage, and cancer location are summarized in Tables S1 and S2. Our analysis focused on patients with microsatellite stable (MSS) colorectal tumors, which was confirmed using standard immunohistochemistry for MLH1, MSH2, MSH6, and PMS2. At the time of resection, matching normal tissues were retrieved at least 5 cm away from the tumor. Upon tissue isolation, both tumor and matching normal tissues were separated into specimens for mechanical testing, histological analysis, and organoid preparation. Tissue sections from formalin-fixed and paraffin-embedded (FFPE) were stained with Hematoxylin and Eosin (H&E) and evaluated by a board-certified pathologist (ZC) in the Department of Pathology at UT Southwestern.

Multiscale biomechanical testing. Specimens for ex vivo mechanical evaluation were frozen at -80˚C and stored until testing. Preliminary experiments ensured that fresh and frozen tissues were mechanically indistinguishable. After thawing each patient sample in a water bath (37˚C), we used a biopsy punch to isolate two to three cylindrical specimens (3 mm in diameter) per sample. The resulting tissue plugs were subjected to mechanical testing using a commercial system (Cell Scale, Waterloo, ON, Canada) and established protocols (*44*, *45*) to determine their material properties at different length scales. All calculations, group averaging, plotting, and biomechanical modeling were carried out using MATLAB R2024b (Mathworks, Natick, MA), unless otherwise specified. Each specimen was subjected to four local indentation tests and to one

global unconfined compression. In both indentation and compression testing, the forces generated by tissues were estimated by measuring the deflection of a microbeam of known elastic modulus (411 GPa) and length (57–59 mm). The microbeam diameter Φ dictates its overall force resolution. Therefore, a smaller diameter was used for local indentation tests (Φ = 0.0762, 0.1016, or 0.1524 mm) while a larger diameter was used for global compression tests (Φ = 0.3048, 0.4064, or 0.5588 mm). The precise microbeam diameter Φ that best matches individual tissue properties was determined via preliminary tests for each specimen. Prior to each experiment, the indenter and compression platen were incubated in 1% bovine serum albumin (BSA) for 30 minutes to minimize tissue adhesion.

Local indentation. A short microbeam of diameter Φ = 0.0762 mm was fixed at the end of the longer force-sensing microbeam in a 90˚ configuration, thus resulting in a cylindrical indenter (cf. Fig. 1C-D). Indentation testing was performed in 5 incremental steps, each with a magnitude equal to 1% of the original height of the sample and interspersed with 1-minute hold phases (Fig. S2A-D). Steady state force (F) values from the hold phases were graphed versus displacement (δ) and fitted using the classical Sneddon's solution from linear elasticity (*94*, *95*),

$$F = E\left(\frac{2R}{1-\nu^2}\right)\delta, \tag{1}$$

where E represents the unknown Young's modulus, R = 38.1 μm is the radius of the cylindrical indenter and ν = 0.5 is the Poisson's ratio for an incompressible linear material. Using this method the calculated values of E indicate the local material properties of human colorectal tissues.

Global compression. A square platen with area 6mm × 6mm was fixed to the force-sensing microbeam, thereby enabling compression of entire specimens (Fig. S3A-C). Since the mechanical behavior of soft tissues is pseudoelastic (*96*), we employed a preconditioning protocol involving 10 cycles of compression up to a deformation of 20% of the initial height of the cylindrical

specimen with a strain rate of 0.5 % / s to yield consistent behaviors under loading. Unconfined compression testing was subsequently performed in 8 incremental steps, each with a magnitude equal to 2.5% (for a total of 20% deformation) interspersed with 2-minute hold phases (Fig. S3D). In addition to enabling force estimation by measuring the microbeam deflection, the side camera allowed us to quantify the specimen geometry (i.e., height and diameter) at each time point during the test (Fig. S3E). Measurements of initial height (H_0) and radius (R_0) of the undeformed specimen and of current tissue height (h_c) and radius (r_c) of the deformed specimen allowed us to calculate radial and axial strain components as $\varepsilon_{rr} = \left(r_c / R_0\right) - 1$ and $\varepsilon_{zz} = \left(h_c / H_0\right) - 1$, respectively. Finally, the axial Cauchy stress was calculated as $\sigma = F / (\pi r_c^2)$. The true Poisson's ratio $\nu = -\varepsilon_{rr} / \varepsilon_{zz}$ was determined by finding the best fit line between the axial and radial strain (Fig. S3F). Steady-state values of the equilibrium Cauchy stress (Fig. S3G-H) were fitted using a neo-Hookean strain energy density function (*97*),

$$W = \frac{c}{2}\left(I_C - 3\right), \tag{2}$$

where c represents an unknown material parameter, and I_C represents the first invariant of the Cauchy-Green tensor. Details regarding parameter estimation via nonlinear least square minimization can be found elsewhere (*44*). To enable comparisons between local and global experiments, the global Young's modulus was determined as $E = 2c\left(1+\nu\right)$, where the values for c and ν where independently estimated for each specimen from unconfined compression data.

Viscoelastic modeling. To fully capture the nonlinear stress-relaxation behavior displayed by colorectal tissues under compression, we implemented a modified Maxwell-Wiechert model (*46*, *47*). Such model consists of a nonlinear spring in parallel to two Maxwell elements, each

consisting of a linear spring and a linear dashpot, as shown in the model schematic (Fig. S4A-B). According to this model, the time-dependent stress response of tissue plugs under compression can be described by the following equation,

$$\sigma_i(t) = \sigma_i^0 + \sum_{j=1}^{2} \sigma_{ij}(t), \tag{3}$$

where $i = 1, \ldots, 8$ indicates each of the loading steps and $j = 1, 2$ indicates each of the Maxwell elements. The stress response of the nonlinear spring σ_i^0 is described by the following equation,

$$\sigma_i^0 = c_a \exp(c_b \varepsilon_i) \varepsilon_i, \tag{4}$$

where c_a is a stress-like material parameter quantifying the stiffness of the nonlinear spring and c_b represents a dimensionless parameter indicating the nonlinearity of the stress-strain response. The symbol ε_i indicates the discrete values taken by the axial strain component ε_{zz} at the end of each stress-relaxation step *i*. Finally, the stress response by the Maxwell elements $\sigma_{ij}(t)$ is described by the following equations, valid for each compression step ($t_i \le t \le t_{i+1}$):

$$\sigma_{ij}(t) = c_m \varepsilon_{ij}^s(t), \tag{5a}$$

$$\varepsilon_{ij}^s(t) = \frac{\eta_j \hat{\varepsilon}_{ij}^s}{\eta_j + \hat{\varepsilon}_{ij}^s c_m (t - t_i)}, \tag{5b}$$

$$\hat{\varepsilon}_{ij}^s = (\varepsilon_i - \varepsilon_{i-1}) + \varepsilon_{(i-1)j}^s(t)\Big|_{t=t_i}, \tag{5c}$$

where c_m is a stress-like material parameter quantifying the stiffness of the linear spring while η_j (with $j = 1, 2$) are the coefficient of viscosity (with units of stress × time) for standard dashpots indicating the amount of viscous damping. Following Tuttle at al. (*47*), we assume that the two Maxwell elements have the same stiffness c_m but different viscosities η_1 and η_2. The symbol

$\varepsilon_{ij}^{s}(t)$ indicates the strain experienced at the *i*-th compression step by the spring within the *j*-th Maxwell element. Equation (5) is solved under the following initial conditions: $\varepsilon_0 = 0, \varepsilon_{0j}^{s}(t_1) = 0$. Details regarding model parameters and their numerical estimation can be found elsewhere (*47*). Briefly, a two-step fitting procedure was employed: parameters for the nonlinear spring (c_a and c_b) were determined by fitting equilibrium data (Fig. S4C), while the parameters for the Maxwell elements (c_m, η_1, and η_2) were determined by fitting transient responses (Fig. S4D).

Quantitative histology. Histological examination of human colorectal tissues was conducted using FFPE blocks sectioned at 4 µm, and stained using Masson's Trichrome (MTC), and Picrosirius Red (PSR). Histology slides were imaged using a Nikon TI2-E inverted microscope equipped with a DS-RI2 color CMOS camera (Nikon, Tokyo, Japan) and custom analyzer and polarizer filters. Complete cross-sectional views of the stained tissues were obtained by acquiring images using a 4× objective and by stitching individual images using the NIS-Elements software. Tiled images were acquired using the following settings: 2424 × 2424 pixels at a resolution of 0.734 µm/pixel, and a 15% overlap. For each image, five representative regions (1 mm × 1 mm) were cropped and processed independently. The resulting images were analyzed using a custom MATLAB script described elsewhere (*50*, *51*, *98*) to quantify the area fractions of collagen from MTC images and to identify the fraction of thick (red), intermediate (orange-yellow), or thin (green) birefringent collagen fibers from PSR images. Briefly, image analysis first consisted of global thresholding to saturate the background to a uniform white (for MTC staining) or black (for PSR staining) value and to eliminate variations in background illumination. Pixel-specific thresholding was performed in the HSL (hue–saturation–lightness) color space. Specifically, blue pixels from MTC images (H = 150 – 249˚, S = 0 – 1, and L = 0.01 – 1) were classified as total

collagen. Collagen of varying thickness was identified from PSR images by separating the hue of red (H = 324 – 12˚), orange (H = 13 – 52˚), yellow (H = 53 – 72˚), and green (H = 73 – 180˚) pixels while keeping saturation and lightness fixed (S = 0.1 – 1, and L = 0.1 – 0.93). Results are reported in terms of area fractions, by computing the ratio of positively identified pixels to total number of pixels in the tissue sections.

Multiphoton microscopy. The architecture of fibrous collagen was captured by imaging H&E-stained slides with a FV MPE-RS multiphoton microscope (Olympus, Tokyo, Japan) in the UT Dallas Imaging & Histology core. The laser beam (Mai-Tai HP DeepSee, Spectra Physics, Santa Clara, CA) was focused on the slides through a 25× water-immersion objective (Olympus, 1.05 N.A., 2 mm working distance) mounted in upright configuration. Following prior work (*44*, *45*), we used an excitation wavelength of 880 nm and collected the second harmonic generation (SHG) signal from the collagen matrix using a 410-455nm bandpass filter. Tiled image stacks were acquired using the following settings: 512 × 512 pixels at a resolution of 0.994 µm/pixel, a pixel dwell time of 2 µs, a stack size of 30 µm with 5 µm steps, and a 10% overlap. The resulting SHG images of whole tissue cross-sections were analyzed using the ImageJ plugin Ridge Detection (*57*), alongside a custom written MATLAB script. For each image, five representative regions (1 mm × 1 mm) were cropped and processed independently. For each region, the average signal intensity was calculated by averaging the SHG signal intensity across all pixels. The images were then converted to an 8-bit format and analyzed using the following setting for Ridge Detection: line width = 3, high contrast = 100, low contrast = 10, lower threshold = 0.34, upper threshold = 4.25, minimum line length = 0, maximum line length = 100. Individual fibers in the regions were detected as ridges, and the fiber length and width were calculated and reported based on the means of detected ridge dimensions per image (Fig. S7). To quantify fiber orientation, an Orientation

Index (*OI*) was defined as $OI = 1 - \sqrt{\text{circular variance}}$, where the circular variance was calculated using the *circ_var* function of the CircStat MATLAB toolbox (*99*). The circular variance measures the directional spread of fiber angles, ranging from 0 (all fibers aligned) to 1 (completely random orientation). Consequently, the Orientation Index ranges from 0 for randomly oriented fibers to 1 for perfectly aligned fibers.

Spatial transcriptomics. We quantified local RNA expression with spatial context using the GeoMx® RNA assay (*67*, *68*). Steps in the experimental and analysis pipeline are described in detail below.

Sample preparation. Three sporadic EO CRC and three sporadic AO CRC samples, along with matching normal tissues were selected based on age at resection and on inclusion of both epithelial and stromal content with verification by our pathologist (ZC; see patient characteristics for those included in this analysis in Tables S1 and S2). Fresh cuts of 5 µm FFPE sections were mounted on charged slides, baked, and stained using the BOND RX/RXm Fully Automated IHC/ISH Stainer from Leica Biosystems, following the manufacturer's automated slide preparation user manual. Immunofluorescent labeling of distinct cell compartments was conducted using the following markers: epithelial cells via pan-cytokeratin (PanCK, Novus NBP2-33200AF532-AF532; 1:40); non-immune stromal cells via vimentin (Santa Cruz sc373717-AF594, 1:150); leukocytes via CD45 (Nanostring CD45-AF647, clone D9M8I, CST cat number 13917; 5 µg/ml), cell nuclei via SYTO13 (Nanostring; 1:10). After staining, all slides were immediately scanned. In total, 72 regions of interest (ROI) were selected, including: AO Matched Normal (6 for Vimentin), AO Cancer (9 for PanCK, and 17 for Vimentin), EO Matched Normal (7 for Vimentin), EO Cancer (10 for PanCK, and 23 for Vimentin). Section AO2 did not have a matched normal and

could not be used due to technical compromise. Overall, 59 ROIs from cancers and 13 from matched normal tissues were selected for extraction and sequencing.

Digital spatial profiling. After hybridization with RNA probes conjugated to barcoded oligonucleotide tags with an ultraviolet (UV) photocleavable linker and staining with fluorescent morphology markers (PanCK, Vimentin, CD45, SYTO13), the slides were loaded onto a GeoMx® (NanoString Technologies, Seattle, WA, USA) digital spatial profiler (DSP) and scanned. The labeled tissues were imaged, and specific regions of interest (ROIs) were selected based on cellular localization and fluorescent tagging. ROIs were chosen to contain at least 30 nuclei, delimited by the morphological markers and the accompanying fluorochrome. Some ROIs were further segmented into more areas of illumination (AOI) based on segmentation of morphological markers. Finally, the selected AOIs were successively exposed to UV light, and the barcoded oligos were released, aspirated, and dispensed into a collection plate for library preparation for next-generation sequencing (NGS). The isolated RNA was subjected to bulk RNA-sequencing.

Library preparation and sequencing. The NGS libraries were prepared following the NanoString GeoMx pipeline. In brief, after the collection was complete, aspirates in the collection plate were dried at 65°C for 1 hour in a thermal cycler with the lid open and resuspended in 10 μL of nuclease-free water. 4 μL of rehydrated aspirates were mixed with 2 μL of 5×PCR Master Mix and 4 μL of SeqCode primers, and PCR amplification with 18 cycles was performed. The PCR products were then pooled equally and purified twice with 1.2×AMPure XP beads (Beckman Coulter, Brea, CA, USA). The final libraries were evaluated and quantified using Agilent's high-sensitivity DNA kit and Invitrogen's Qubit dsDNA HS assay, respectively. Total sequencing reads per DSP collection plate were calculated using the NanoString GeoMx worksheet. The libraries

were subjected to 2×38 bp paired-end sequencing on an Illumina NovaSeq 6000 system with a 100-cycle S1 kit.

Bulk RNA-seq data analysis. We used the Nanostring GeoMx Human Whole Transcriptome Atlas (WTA) platform to profile 72 ROIs from all slides. This panel profiles the whole transcriptome by targeting 18,677 unique transcripts from human protein-encoding genes plus ERCC negative controls. The panel excludes uninformative high-abundance RNAs such as ribosomal subunits and includes RNA probes designed for Illumina NGS readout with the Seq Code library prep. Digital count conversion (DCC) files were generated using the GeoMx® NGS Pipeline (Version 2.3.3.10) from FASTQ sequencing files and uploaded into the GeoMx DSP Data Analysis Suite for spatially resolved expression analysis and visualizations. Standard quality control was carried out using default settings per the manufacturer's guidelines. All 72 segments passed quality control analysis. Gene filtering retained 14,364 out of 18,677 genes (76.94%) after removing targets with expression at or lower than the selected threshold value at or above specific frequency (5% in our case). Q3 normalization was applied to account for differences in sequencing yield, enabling biological comparison of gene expression across the segments. The normalized count density distributions across individual segments were grossly similar, and there was no observable bias by either pathologic grade or epithelial histology.

Differential expression analysis between groups was performed using the *limma* package in R (version 4.4.3) after log2 transformation (with a pseudocount of 1) of the pre-normalized expression data. To maintain the spatial resolution inherent in the GeoMx data while accounting for patient effects, we implemented a ROI-level analysis that treated individual ROIs as observations while incorporating patient IDs as covariates in the statistical model. A linear model was fitted with patient onset type (EO vs. AO) as the main effect of interest and patient ID as a

covariate to account for within-patient correlation. This approach preserves spatial heterogeneity information while controlling for patient-specific effects. An empirical Bayes method was used to moderate the standard errors of the estimated log-fold, thus resulting in more stable inference and improved power, especially considering the small numbers of samples. Differentially expressed genes were identified using thresholds of adjusted p-value < 0.05 and absolute log2 Fold Change > 1.0. To adjust for multiple testing, Benjamini and Hochberg (*100*) method was used to control false discovery rate (FDR). Pathway enrichment analysis was performed using Gene Ontology (GO) gene sets and was implemented with the *clusterProfiler* package using the org.Hs.eg.db annotation database for gene identifier mapping. Significantly enriched pathways were identified using a p-value threshold of 0.05 and a q-value (FDR) threshold of 0.1. For the epithelial compartment, we performed a comprehensive pathway analysis using the Correlation Adjusted MEan RAnk gene set test (CAMERA) (*101*). Eight distinct mechanotransduction-related gene sets were curated to represent key functional modules of cellular mechanosensing: (1) mechanosensors (ion channels and transmembrane proteins that directly sense mechanical forces); (2) focal adhesion and cell-ECM adhesion proteins; (3) integrins; (4) cytoskeletal components; (5) Rho GTPase signaling proteins; (6) LINC complex components; (7) Hippo pathway components; and (8) mechanosensitive transcription factors (Mechano TFs). For each mechanotransduction gene set, CAMERA calculated a competitive gene set test statistic that evaluated whether genes in the set were more highly differentially expressed between EO and AO samples compared to genes outside the set. Finally, Gene Set Enrichment Analysis (*102*) was conducted using the GSEA (v14) algorithm (https://www.gsea-msigdb.org/gsea/index.jsp). Expression patterns were visualized using the R functions *ggplot2*. Correlation analysis between ECM genes was performed using Spearman's rank correlation. Visualizations were optimized for publication quality, with consistent

color schemes, with red indicating genes upregulated in EO CRC and blue indicating genes upregulated in AO CRC.

Cell segmentation and phenotype identification. To achieve a better understanding of the structural and functional relationships between epithelial and stromal cell populations, we used the high-resolution immunofluorescence images acquired for DSP to conduct single-cell segmentation of human CRC tissues. First, immunofluorescence images were annotated using DeepCell Label (*103*), a browser-based graphical user interface for editing cell annotations and for training the neural network for single-cell segmentation. Next, we used Mesmer (*59*), a deep-learning algorithm to generate automated whole-cell and nuclear boundaries. Briefly, we used nuclear images (SYTO13) to identify the nucleus of each cell, while we used cytoplasmic images (PanCK, Vimentin) to define the area occupied by each cell. Because of the low intensity in the CD45 channel in all images, we decided to exclude the immune marker from this analysis thus avoiding erroneous segmentations. The deep-learning model produces predictions for the centroid and boundary of each nucleus and cell captured in the original image. This method allowed us to segment 2,155,046 cells from 11 patient-derived samples. After segmentation, single-cell morphological features (area, major and minor axis length, eccentricity, solidity, extent, and orientation) and fluorescence intensity of each marker were extracted using the *scikit-image* Python library. The cell aspect ratio was calculated by dividing the length of the major axis by the length of the minor axis. All features were z-score normalized (*104*) across the dataset to facilitate cross-sample comparison of marker expression (PanCK and Vimentin) across groups and to enable clustering analysis. Finally, we identified distinct cellular phenotypes via unsupervised Louvain clustering (*60*) which was implemented using the Python library *Scanpy* (*105*). We first constructed a k-nearest neighbor (KNN) graph based on Euclidean distances computed from the

z-normalized feature space, including both morphological features and marker intensities. A resolution of 0.1 was chosen to avoid over-clustering and to identify major cell phenotypes with robust morphological and marker-based separation. Using this approach, we found that all cells within our dataset clustered into four groups. Depending on the average marker expression and the average cell area, the four clusters were assigned to the following cell types: epithelial large (high PanCK, low Vimentin, high cell area), epithelial small (high PanCK, low Vimentin, low cell area), stroma (low PanCK, high Vimentin, high cell area), immune (low PanCK, high Vimentin, low cell area). These four phenotypes were validated by superimposing the cell cluster labels on the original immunofluorescence images (Fig. S9A-D).

Immunofluorescence and immunohistochemistry. Staining for YAP in human colorectal tissues was conducted using FFPE blocks sectioned at 4 µm (prepared by the Tissue Management Shared Resources at UT Southwestern). Tissue sections were deparaffinized and subjected to antigen retrieval using a tris/borate/EDTA buffer (pH 9.0). The slides were cooled to room temperature and washed twice with PBS. Sections were incubated in 0.3% H_2O_2 in PBS for 10 minutes at room temperature and then blocked with 10% serum and permeabilized with 0.3% Triton X-100 in PBS for 15 minutes at room temperature. The slides were stained with anti-active-YAP1 (Abcam, ab205270, 1:2000) at 4˚C overnight. The next day, slides were incubated at room temperature for 1 hour before being washed three times with PBS and incubated with AF594 conjugated secondary antibody (Invitrogen, A32740, 1:1000) for 1 hour at room temperature. After three rounds of PBS wash, slides were incubated with DAPI (1:2000 in PBS) for 15 minutes at room temperature. Lastly, slides were mounted using Prolong Gold Antifade (Invitrogen P36931). Slides were kept in the dark at 4˚C and dried overnight. Images were captured using an automated widefield epifluorescence slide scanner with LED excitation (Zeiss Axioscan.Z1) at 20× by the

Whole Brain Imaging Core at UT Southwestern. A custom ImageJ macro was developed to isolate epithelial regions manually using a brush tool to exclude non-epithelial cells from subsequent analyses. Nuclear regions in the epithelium were identified by DAPI thresholding (intensity thresholds: 75-255) and the fluorescent intensity of nuclear Active YAP was quantified only within the nuclear compartment of individual cells.

Staining for Ki67 in human colorectal tissues was conducted using FFPE blocks sectioned at 4 μm obtained from the Tissue Management Shared Resource core at UT Southwestern following standard protocols (*106*). Tissue sections were deparaffinized and subjected to antigen retrieval using a sodium citrate buffer containing 0.05% Triton X-100 (pH 6.0). Slides were stained using an antibody for Ki67 (Proteintech 27309-1-AP, 1:5000) and imaged using a Whole Slide Scanner (NanoZoomer by Hamamatsu) at 20× magnification. Ki67+ cells were quantified using an automatic cell detection tool in QuPath-v0.5.0 (*107*), an open source software for digital pathology image analysis. Briefly, IHC image files were opened in QuPath as Brightfield H-DAB images. Epithelial cancer cell regions were selected using the brush tool. QuPath's Positive Cell Detection tool was used to quantify the number of DAB positive nuclei (Ki67+) on cancer regions using the Hematoxylin OD image as the detection image.

Cell culture experiments. Polyacrylamide (PA) gels were prepared by mixing solutions of 40% acrylamide and 2% bis-acrylamide (Bio-Rad, Hercules, CA) using established protocols (*108*, *109*). Briefly, the bottom of 12-well glass bottom plates (Cellvis P12-1.5H-N) was treated with 1 mL of bind silane solution (80 μL glacial acetic acid, 50 μL 3-(trimethoxysilyl)propyl methacrylate, and 200 mL deionized water) for 1 hour at room temperature. Glass bottom plates were then rinsed thoroughly with distilled water and dried with an air gun. Top coverslips (18 mm in diameter) were passivated by treating them with 0.1 M NaOH for 1 hour at room temperature,

rinsed three times with deionized water, and then dried with compressed N_2. Soft PA gels consisted of 75 μL acrylamide and 24 μL bis-acrylamide, while stiff gels were prepared by mixing 188 μL acrylamide and 19 μL bis-acrylamide. In both cases, 0.5 μL TEMED and 100 μL of 5% ammonium persulfate (APS) solution were added, and sterile deionized water was added to achieve a 1 mL solution. A 200 μL droplet was placed in each well and covered with a passivated coverslip to spread the liquid uniformly across the bottom of the well. The PA was allowed to polymerize for 30 minutes under vacuum and the top coverslip was carefully removed by using fine forceps. We assessed the mechanical properties of the resulting PA gels using the unconfined compression protocol described above. Polymerized PA gels were first treated with 440 μL of a 1:50 (v/v) mixture of Sulfosuccinimidyl 6-(4'-azido-2'-nitrophenylamino)hexanoate (Sulfo-SANPAH) (ProteoChem) and 50 mM HEPES solution under a UV light for 10 min. PA gels were subsequently incubated in either 0.2 mg/mL collagen I (Corning, 354249) or 1.5% growth-factor reduced Matrigel (Corning, 354230) at 37˚C for 30 minutes. The colon cancer lines HT29 (ATCC, HTB-38, 44-year-old female) and SW480 (ATCC, CCL-228, 50-year-old male) were cultured in DMEM (Corning, 10013CV), supplemented with 10% fetal bovine serum (ATCC, 302020) and 1% penicillin/streptomycin (ATCC, 302300). Both cell lines were authenticated by short-tandem repeat profiling using a commercial kit (ATCC, 135-XV). Cell cultures were maintained in humidified incubators at 37˚C and 5% CO_2 in T75 flasks and were monitored regularly under a phase contrast microscope. Cells were routinely tested for mycoplasma contamination using the MycoAlert kit (Lonza, LT07-218) to ensure that cultures remained contamination-free. At the time of passage, HT29 cells were seeded at a density of 50×10^3 cells/cm^2 while SW480 cells were seeded at a density of 40×10^3 cells/cm^2 due to their different rates of proliferation. Cells were allowed to grow on PA gels for one day and then cultured in serum-free DMEM. After 72 hours

of culture on PA gels of varying stiffnesses, cells were fixed using 4% paraformaldehyde (PFA) in PBS for 15 minutes, permeabilized using 0.2% Triton X-100 for 15 minutes and blocked using 2.5% normal horse serum for 15 minutes. Samples were stained with Alexa Fluor 647 phalloidin (Invitrogen, A22287, 1:1000) and DAPI (Invitrogen, D1306, 1:1000). Cell proliferation was assessed using the Click-iT EdU Cell Proliferation Kit (Thermo Fisher, C10637). Briefly, a 2x working solution of EdU (Component A) was prepared in serum-free DMEM and added by replacing 500 μL of medium in each well. After incubation, cells were fixed with 4% PFA for 15 minutes, permeabilized with 0.2% Triton X-100 for 15 minutes and washed thoroughly with PBS. The Click-iT reaction cocktail containing Alexa Fluor 488 azide was prepared according to manufacturer's protocol, and 200 μL was added to each gel surface for 30 minutes at room temperature, protected from light to enable click chemistry detection of incorporated EdU. For visualization, samples were counterstained with DAPI (Invitrogen, D1306, 1:1000).

Quantitative confocal microscopy. Fixed and stained samples were imaged using a Nikon AX confocal microscope and a line series acquisition mode to minimize crosstalk between the 4 fluorescent channels: 405nm excitation / 420-470nm emission (DAPI), 488nm excitation / 500-530nm emission (EdU), 640nm excitation / 660-750nm emission (Phalloidin), and transmitted detector for differential interference contrast (DIC) imaging. Image stacks were acquired using the following settings: 2x line averaging, 1024 × 1024 pixels at a resolution of 0.576 μm/pixel in x-y, 11 z-slices with 11μm step size covering 121μm total depth. Once acquired, each stack was transformed into a maximum intensity projection image and the individual channels were analyzed using fully automated ImageJ macros. For cell proliferation analysis, maximum intensity projections were thresholded (DAPI: 50-255, EdU: 100-255) followed by watershed segmentation and particle analysis (size: 50-50,000 μm^2) to identify total nuclei and proliferating cells. The

proliferation index was calculated as the percentage of EdU-positive nuclei to total DAPI-positive nuclei. Cell morphology was quantified using a custom ImageJ macro to outline the phalloidin-positive cytoplasmic region of individual cells using manual tracing with a polygon tool. For each cell, the aspect ratio was calculated by dividing the length of the major axis by the length of the minor axis. A minimum of 12 cells per region of interest were analyzed. Image processing and analysis were performed using custom ImageJ scripts. For each experimental condition, 6 biological replicates were analyzed with a minimum of 100 cells per replicate to ensure statistical robustness.

Organoid experiments. Human CRC patient-derived organoids were established as described previously (*82*, *83*). Three sporadic EO CRC and three sporadic AO CRC samples were selected based on age at resection and ability to be expanded in vitro (see patient characteristics for those included in this analysis in Tables S1 and S2). Briefly, cells isolated from surgically resected colorectal cancer specimens were plated in Matrigel (Corning, 354230) in 24-well Nunclon Delta plates (ThermoFisher, 142475). Following Matrigel polymerization, the organoids were overlaid with 500 µL of "complete" medium composed of advanced DMEM/F12 (Gibco, 12634) supplemented with 20% FBS, L-WRN medium, 100x GlutaMAX™ (Gibco, 35050), SB431542 (Tocris, 1614), Y27632 (Tocris, 1254) and 1% penicillin/streptomycin (Gibco, 15140). Organoid cultures were maintained in humidified incubators at 37 °C with 5% CO_2 and were monitored regularly under a phase contrast microscope. The culture medium was changed every 2 days. All organoid models were authenticated by short-tandem repeat profiling at the UT Southwestern Genomics Core via the PowerPlex Fusion System and were regularly tested for mycoplasma contamination via the MycoAlert kit (Lonza, LT07-710). Patient-derived organoids were encapsulated in 25 µL Tyramine-Substituted Hyaluronate (TS-HA; synthesized at the

Cleveland Clinic) (*83*). Two TS-HA concentrations (2.5 mg/mL and 8 mg/mL) were used to make hydrogel beads. Briefly, 10^3 organoids were washed with PBS and resuspended in 24 µL of activated TS-HA at room temperature. The TS-HA solution was activated by addition of Horseradish Peroxidase (Sigma-Aldrich; cat# P8250-5KU; at 1:500 ratio). Sterile 12 well silicon isolators (Sigma-Aldrich; cat# GBL665506) of 25 µL each were used as molds for individual beads. TS-HA crosslink reaction with 1 µL of 0.03% hydrogen peroxide was achieved individually in-well. Hydrogel beads were washed with organoid media and incubated at 37˚C in a 5% CO2 incubator for 20 to 30 minutes to remove residual chemicals, followed by a medium change. Beads were used for experiments within 48 hours. A CellTiter-Glo® 3D Cell Viability assay (Promega, G9681) was used to measure viability of encapsulated organoids in TS-HA at both 2.5 mg/mL and 8 mg/mL from both AO and EO CRC patients. Briefly, organoid-containing hydrogel beads were incubated overnight in multi-well clear-bottom opaque plates. CellTiter-Glo® 3D Reagent was added equal to the volume of cell culture medium present in each well. After vigorous shaking, plates were incubated at room temperature for an additional 25 minutes to stabilize the luminescent signal. Luminescence was recorded using a Molecular Devices Spectramax (Model ID3) plate reader. To account for patient-to-patient variability, raw luminescence readings acquired from a given patient organoids were normalized with respect to the lowest reading on soft (2.5 mg/mL) TS-HA hydrogels. This approach allowed us to quantify relative changes in cell viability.

Short-tandem repeat (STR) fingerprinting. Short-tandem repeat analysis was conducted to confirm that patient-derived organoids cultured in vitro preserved the same genomic identity as the corresponding FFPE tissues (Supplemental Table S3). Once established, the organoid DNA isolate (DNeasy Blood & Tissue Kit, Qiagen 69506) was compared to genomic DNA isolated from the companion FFPE sections (GeneRead DNA FFPE Kit Qiagen 180134) and subjected to

analyses at the University of Texas Southwestern McDermott Center Sequencing Core (Department Eugene McDermott Center for Human Growth and Development) to confirm the unique origin of each primary epithelial organoid prior to use in 3D culture assays.

Statistical analysis. Experimental data are presented as mean ± SEM, as box plots, or as violin plots with individual data points showing independent measurements. No statistical method was used to predetermine sample size, and investigators were not blinded during experiments or outcome assessment. Data normality was assessed using the Shapiro-Wilk test and density plots, which revealed non-normal distribution patterns. The Scheirer-Ray-Hare test was used as a non-parametric alternative to two-way ANOVA to assess differences between: (i) cancer and matched normal samples and between AO and EO tissues; (ii) cell lines based on ligand adhesion (Collagen vs. Matrigel) and PA stiffness (Soft, Intermediate, Stiff, and Glass) on cell proliferation; and (iii) organoid viability between AO and EO organoids cultured in TS-HA hydrogels of tunable stiffness (Soft vs. Stiff). Additionally, a Kruskal-Wallis test was employed to determine significant differences in cell aspect ratio and in the fraction of EdU-positive nuclei across three PA stiffnesses (Soft, Stiff, and Glass). For post-hoc multiple comparisons, Dunn's test with Bonferroni correction was used to identify significant differences between specific groups. Results were considered statistically significant at $p < 0.05$. All analyses were performed using R (version 4.4.3).

REFERENCES

1. R. L. Siegel, N. S. Wagle, A. Cercek, R. A. Smith, A. Jemal, Colorectal cancer statistics, 2023. *CA: A Cancer Journal for Clinicians* **73**, 233–254 (2023).

2. R. L. Siegel, T. B. Kratzer, A. N. Giaquinto, H. Sung, A. Jemal, Cancer statistics, 2025. *CA: A Cancer Journal for Clinicians* **75**, 10–45 (2025).

3. H. Sung, R. L. Siegel, M. Laversanne, C. Jiang, E. Morgan, M. Zahwe, Y. Cao, F. Bray, A. Jemal, Colorectal cancer incidence trends in younger versus older adults: an analysis of population-based cancer registry data. *The Lancet Oncology* **26**, 51–63 (2025).

4. B. K. Edwards, E. Ward, B. A. Kohler, C. Eheman, A. G. Zauber, R. N. Anderson, A. Jemal, M. J. Schymura, I. Lansdorp-Vogelaar, L. C. Seeff, M. van Ballegooijen, S. L. Goede, L. A. G. Ries, Annual report to the nation on the status of cancer, 1975-2006, featuring colorectal cancer trends and impact of interventions (risk factors, screening, and treatment) to reduce future rates. *Cancer* **116**, 544–573 (2010).

5. M. Giannakis, K. Ng, A common cancer at an uncommon age. *Science* **379**, 1088–1090 (2023).

6. C. L. S. Molmenti, E. T. Jacobs, S. Gupta, C. A. Thomson, Early-Onset Colorectal Cancer: A Call for Greater Rigor in Epidemiologic Studies. *Cancer Epidemiology, Biomarkers & Prevention* **31**, 507–511 (2022).

7. C. E. Bailey, C.-Y. Hu, Y. N. You, B. K. Bednarski, M. A. Rodriguez-Bigas, J. M. Skibber, S. B. Cantor, G. J. Chang, Increasing Disparities in the Age-Related Incidences of Colon and Rectal Cancers in the United States, 1975-2010. *JAMA Surgery* **150**, 17–22 (2015).

8. E. M. Montminy, M. Zhou, L. Maniscalco, R. Heda, M. K. Kim, S. G. Patel, X.-C. Wu, S. H. Itzkowitz, J. J. Karlitz, Shifts in the Proportion of Distant Stage Early-Onset Colorectal Adenocarcinoma in the United States. *Cancer Epidemiology, Biomarkers & Prevention* **31**, 334–341 (2022).

9. L. J. Hofseth, J. R. Hebert, A. Chanda, H. Chen, B. L. Love, M. M. Pena, E. A. Murphy, M. Sajish, A. Sheth, P. J. Buckhaults, F. G. Berger, Early-onset colorectal cancer: initial clues and current views. *Nat Rev Gastroenterol Hepatol* **17**, 352–364 (2020).

10. A. M. D. Wolf, E. T. H. Fontham, T. R. Church, C. R. Flowers, C. E. Guerra, S. J. LaMonte, R. Etzioni, M. T. McKenna, K. C. Oeffinger, Y.-C. T. Shih, L. C. Walter, K. S. Andrews, O. W. Brawley, D. Brooks, S. A. Fedewa, D. Manassaram-Baptiste, R. L. Siegel, R. C. Wender, R. A. Smith, Colorectal cancer screening for average-risk adults: 2018 guideline update from the American Cancer Society. *CA: A Cancer Journal for Clinicians* **68**, 250–281 (2018).

11. US Preventive Services Task Force, Screening for Colorectal Cancer: US Preventive Services Task Force Recommendation Statement. *JAMA* **325**, 1965–1977 (2021).

12. D. T. Chang, R. K. Pai, L. A. Rybicki, M. A. Dimaio, M. Limaye, P. Jayachandran, A. C. Koong, P. A. Kunz, G. A. Fisher, J. M. Ford, M. Welton, A. Shelton, L. Ma, D. A. Arber, R. K. Pai, Clinicopathologic and molecular features of sporadic early-onset colorectal adenocarcinoma: an adenocarcinoma with frequent signet ring cell differentiation, rectal and sigmoid involvement, and adverse morphologic features. *Modern Pathology* **25**, 1128–1139 (2012).

13. P. J. Limburg, D. W. Mahoney, D. A. Ahlquist, H. T. Allawi, S. C. Johnson, M. Kaiser, V. E. Katerov, S. Statz, R. P. Graham, P. H. Foote, K. A. Doering, K. N. Burger, G. P. Lidgard, J. B. Kisiel, Comparison of Tissue-Based Molecular Markers in Younger versus Older Patients with Colorectal Neoplasia. *Cancer Epidemiology, Biomarkers & Prevention* **29**, 1570–1576 (2020).

14. A. Cercek, W. K. Chatila, R. Yaeger, H. Walch, G. D. S. Fernandes, A. Krishnan, L. Palmaira, A. Maio, Y. Kemel, P. Srinivasan, C. Bandlamudi, E. Salo-Mullen, P. R. Tejada, K. Belanfanti, J. Galle, V. Joseph, N. Segal, A. Varghese, D. Reidy-Lagunes, J. Shia, E. Vakiani, S. Mondaca, R. Mendelsohn, M. A. Lumish, F. Steinruecke, N. Kemeny, L. Connell, K. Ganesh, A. Markowitz, G. Nash, J. Guillem, J. J. Smith, P. B. Paty, L. Zhang, D. Mandelker, O. Birsoy, M. Robson, K. Offit, B. Taylor, M. Berger, D. Solit, M. Weiser, L. B. Saltz, J. G. Aguilar, N. Schultz, L. A. Diaz Jr,, Z. K. Stadler, A Comprehensive Comparison of Early-Onset and Average-Onset Colorectal Cancers. *JNCI: Journal of the National Cancer Institute* **113**, 1683–1692 (2021).

15. R. N. Lui, K. K. F. Tsoi, J. M. W. Ho, C. M. Lo, F. C. H. Chan, M. H. Kyaw, J. J. Y. Sung, Global Increasing Incidence of Young-Onset Colorectal Cancer Across 5 Continents: A Joinpoint Regression Analysis of 1,922,167 Cases. *Cancer Epidemiology, Biomarkers & Prevention* **28**, 1275–1282 (2019).

16. A. A. Arif, D. Chahal, G. K. Ladua, E. Bhang, B. Salh, G. Rosenfeld, J. M. Loree, F. Donnellan, Hereditary and Inflammatory Bowel Disease-Related Early Onset Colorectal Cancer Have Unique Characteristics and Clinical Course Compared with Sporadic Disease. *Cancer Epidemiology, Biomarkers & Prevention* **30**, 1785–1791 (2021).

17. Y. N. You, Y. Xing, B. W. Feig, G. J. Chang, J. N. Cormier, Young-Onset Colorectal Cancer: Is It Time to Pay Attention? *Archives of Internal Medicine* **172**, 287–289 (2012).

18. E. M. Stoffel, C. C. Murphy, Epidemiology and Mechanisms of the Increasing Incidence of Colon and Rectal Cancers in Young Adults. *Gastroenterology* **158**, 341–353 (2020).

19. R. L. Siegel, K. D. Miller, A. Jemal, Colorectal Cancer Mortality Rates in Adults Aged 20 to 54 Years in the United States, 1970-2014. *JAMA* **318**, 572–574 (2017).

20. C. Eng, A. A. Jácome, R. Agarwal, M. H. Hayat, M. X. Byndloss, A. N. Holowatyj, C. Bailey, C. H. Lieu, A comprehensive framework for early-onset colorectal cancer research. *The Lancet Oncology* **23**, e116–e128 (2022).

21. D. Hanahan, R. A. Weinberg, Hallmarks of Cancer: The Next Generation. *Cell* **144**, 646–674 (2011).

22. H. F. Dvorak, Tumors: Wounds That Do Not Heal—Redux. *Cancer Immunology Research* **3**, 1–11 (2015).

23. M. Schmitt, F. R. Greten, The inflammatory pathogenesis of colorectal cancer. *Nat Rev Immunol* **21**, 653–667 (2021).

24. D. Hanahan, Hallmarks of Cancer: New Dimensions. *Cancer Discov* **12**, 31–46 (2022).

25. D. J. Tschumperlin, G. Ligresti, M. B. Hilscher, V. H. Shah, Mechanosensing and fibrosis. *J Clin Invest* **128**, 74–84 (2018).

26. J. Winkler, A. Abisoye-Ogunniyan, K. J. Metcalf, Z. Werb, Concepts of extracellular matrix remodelling in tumour progression and metastasis. *Nat Commun* **11**, 5120 (2020).

27. M. L. Meizlish, R. A. Franklin, X. Zhou, R. Medzhitov, Tissue Homeostasis and Inflammation. *Annual Review of Immunology* **39**, 557–581 (2021).

28. T. E. Sutherland, D. P. Dyer, J. E. Allen, The extracellular matrix and the immune system: A mutually dependent relationship. *Science* **379**, eabp8964 (2023).

29. M. J. Paszek, N. Zahir, K. R. Johnson, J. N. Lakins, G. I. Rozenberg, A. Gefen, C. A. Reinhart-King, S. S. Margulies, M. Dembo, D. Boettiger, D. A. Hammer, V. M. Weaver, Tensional homeostasis and the malignant phenotype. *Cancer Cell* **8**, 241–254 (2005).

30. A. J. Rice, E. Cortes, D. Lachowski, B. C. H. Cheung, S. A. Karim, J. P. Morton, A. del Río Hernández, Matrix stiffness induces epithelial–mesenchymal transition and promotes chemoresistance in pancreatic cancer cells. *Oncogenesis* **6**, e352–e352 (2017).

31. T. B. Halvorsen, E. Seim, Association between invasiveness, inflammatory reaction, desmoplasia and survival in colorectal cancer. *Journal of Clinical Pathology* **42**, 162–166 (1989).

32. H. Ueno, Y. Kanemitsu, S. Sekine, M. Ishiguro, E. Ito, Y. Hashiguchi, F. Kondo, H. Shimazaki, S. Mochizuki, Y. Kajiwara, E. Shinto, J. Yamamoto, Desmoplastic Pattern at the Tumor Front Defines Poor-prognosis Subtypes of Colorectal Cancer. *The American Journal of Surgical Pathology* **41**, 1506 (2017).

33. A. Caporale, S. A. Bonapasta, M. Scarpini, A. Ciardi, A. Vestri, M. Ruperto, A. Giuliani, Quantitative Investigation of Desmoplasia as a Prognostic Indicator in Colorectal Cancer. *Journal of Investigative Surgery* **23**, 105–109 (2010).

34. V. J. Coulson-Thomas, Y. M. Coulson-Thomas, T. F. Gesteira, C. A. A. de Paula, A. M. Mader, J. Waisberg, M. A. Pinhal, A. Friedl, L. Toma, H. B. Nader, Colorectal cancer desmoplastic reaction up-regulates collagen synthesis and restricts cancer cell invasion. *Cell Tissue Res* **346**, 223–236 (2011).

35. S. Kawano, M. Kojima, Y. Higuchi, M. Sugimoto, K. Ikeda, N. Sakuyama, S. Takahashi, R. Hayashi, A. Ochiai, N. Saito, Assessment of elasticity of colorectal cancer tissue, clinical utility, pathological and phenotypical relevance. *Cancer Science* **106**, 1232–1239 (2015).

36. M. Nebuloni, L. Albarello, A. Andolfo, C. Magagnotti, L. Genovese, I. Locatelli, G. Tonon, E. Longhi, P. Zerbi, R. Allevi, A. Podestà, L. Puricelli, P. Milani, A. Soldarini, A. Salonia, M. Alfano, Insight On Colorectal Carcinoma Infiltration by Studying Perilesional Extracellular Matrix. *Sci Rep* **6**, 22522 (2016).

37. E. Brauchle, J. Kasper, R. Daum, N. Schierbaum, C. Falch, A. Kirschniak, T. E. Schäffer, K. Schenke-Layland, Biomechanical and biomolecular characterization of extracellular matrix structures in human colon carcinomas. *Matrix Biology* **68–69**, 180–193 (2018).

38. E. Lopez-Crapez, L. Costa, G. Tosato, J. Ramos, T. Mazard, J. Guiramand, A. Thierry, J. Colinge, P.-E. Milhiet, C. Bénistant, Mechanical signatures of human colon cancers. *Sci Rep* **12**, 12475 (2022).

39. F. A. Sinicrope, Increasing Incidence of Early-Onset Colorectal Cancer. *New England Journal of Medicine* **386**, 1547–1558 (2022).

40. R. L. Siegel, L. A. Torre, I. Soerjomataram, R. B. Hayes, F. Bray, T. K. Weber, A. Jemal, Global patterns and trends in colorectal cancer incidence in young adults. *Gut* **68**, 2179–2185 (2019).

41. S. Chakraborty, K. E. Peak, J. P. Gleghorn, T. J. Carroll, V. D. Varner, "Quantifying Spatial Patterns of Tissue Stiffness Within the Embryonic Mouse Kidney" in *Tissue Morphogenesis: Methods and Protocols*, C. M. Nelson, Ed. (Springer US, New York, NY, 2024; https://doi.org/10.1007/978-1-0716-3854-5_12), pp. 171–186.

42. K. E. Peak, P. Rajaguru, A. Khan, J. P. Gleghorn, G. Obaid, J. Ferruzzi, V. D. Varner, Photo-induced changes in tissue stiffness alter epithelial budding morphogenesis in the embryonic lung. bioRxiv [Preprint] (2024). https://doi.org/10.1101/2024.08.22.609268.

43. P. Deptuła, D. Łysik, K. Pogoda, M. Cieśluk, A. Namiot, J. Mystkowska, G. Król, S. Głuszek, P. A. Janmey, R. Bucki, Tissue Rheology as a Possible Complementary Procedure to Advance Histological Diagnosis of Colon Cancer. *ACS Biomater. Sci. Eng.* **6**, 5620–5631 (2020).

44. J. Ferruzzi, M. Sun, A. Gkousioudi, A. Pilvar, D. Roblyer, Y. Zhang, M. H. Zaman, Compressive Remodeling Alters Fluid Transport Properties of Collagen Networks – Implications for Tumor Growth. *Sci Rep* **9**, 1–16 (2019).

45. W. Kang, J. Ferruzzi, C.-P. Spatarelu, Y. L. Han, Y. Sharma, S. A. Koehler, J. A. Mitchel, A. Khan, J. P. Butler, D. Roblyer, M. H. Zaman, J.-A. Park, M. Guo, Z. Chen, A. F. Pegoraro, J. J. Fredberg, A novel jamming phase diagram links tumor invasion to non-equilibrium phase separation. *iScience* **24**, 103252 (2021).

46. R. Van Mastrigt, J. C. Nagtegaal, Dependence of the viscoelastic response of the urinary bladder wall on strain rate. *Med. Biol. Eng. Comput.* **19**, 291–296 (1981).

47. T. Tuttle, D. McClintock, S. Roccabianca, Effects of swelling and anatomical location on the viscoelastic behavior of the porcine urinary bladder wall. *Journal of the Mechanical Behavior of Biomedical Materials* **143**, 105926 (2023).

48. L. C. U. Junqueira, G. Bignolas, R. R. Brentani, Picrosirius staining plus polarization microscopy, a specific method for collagen detection in tissue sections. *Histochem J* **11**, 447–455 (1979).

49. D. Dayan, Y. Hiss, A. Hirshberg, J. J. Bubis, M. Wolman, Are the polarization colors of Picrosirius red-stained collagen determined only by the diameter of the fibers? *Histochemistry* **93**, 27–29 (1989).

50. M. R. Bersi, M. J. Collins, E. Wilson, J. D. Humphrey, Disparate Changes in the Mechanical Properties of Murine Carotid Arteries and Aorta in Response to Chronic Infusion of Angiotensin-II. *Int J Adv Eng Sci Appl Math* **4**, 228–240 (2012).

51. J. Ferruzzi, D. Madziva, A. W. Caulk, G. Tellides, J. D. Humphrey, Compromised mechanical homeostasis in arterial aging and associated cardiovascular consequences. *Biomechanics and Modeling in Mechanobiology* **17**, 1281–1295 (2018).

52. R. Lattouf, R. Younes, D. Lutomski, N. Naaman, G. Godeau, K. Senni, S. Changotade, Picrosirius Red Staining: A Useful Tool to Appraise Collagen Networks in Normal and Pathological Tissues. *J Histochem Cytochem.* **62**, 751–758 (2014).

53. A. Zoumi, A. Yeh, B. J. Tromberg, Imaging cells and extracellular matrix in vivo by using second-harmonic generation and two-photon excited fluorescence. *Proceedings of the National Academy of Sciences* **99**, 11014–11019 (2002).

54. E. Brown, T. McKee, E. diTomaso, A. Pluen, B. Seed, Y. Boucher, R. K. Jain, Dynamic imaging of collagen and its modulation in tumors in vivo using second-harmonic generation. *Nature Medicine* **9**, 796 (2003).

55. X. Chen, O. Nadiarynkh, S. Plotnikov, P. J. Campagnola, Second harmonic generation microscopy for quantitative analysis of collagen fibrillar structure. *Nature Protocols* **7**, 654–669 (2012).

56. C. R. Drifka, A. G. Loeffler, K. Mathewson, G. Mehta, A. Keikhosravi, Y. Liu, S. Lemancik, W. A. Ricke, S. M. Weber, W. J. Kao, K. W. Eliceiri, Comparison of Picrosirius Red Staining With Second Harmonic Generation Imaging for the Quantification of Clinically Relevant Collagen Fiber Features in Histopathology Samples. *J Histochem Cytochem.* **64**, 519–529 (2016).

57. C. Steger, An unbiased detector of curvilinear structures. *IEEE Transactions on Pattern Analysis and Machine Intelligence* **20**, 113–125 (1998).

58. M. W. Conklin, J. C. Eickhoff, K. M. Riching, C. A. Pehlke, K. W. Eliceiri, P. P. Provenzano, A. Friedl, P. J. Keely, Aligned Collagen Is a Prognostic Signature for Survival in Human Breast Carcinoma. *The American Journal of Pathology* **178**, 1221–1232 (2011).

59. N. F. Greenwald, G. Miller, E. Moen, A. Kong, A. Kagel, T. Dougherty, C. C. Fullaway, B. J. McIntosh, K. X. Leow, M. S. Schwartz, C. Pavelchek, S. Cui, I. Camplisson, O. Bar-Tal, J. Singh, M. Fong, G. Chaudhry, Z. Abraham, J. Moseley, S. Warshawsky, E. Soon, S. Greenbaum, T. Risom, T. Hollmann, S. C. Bendall, L. Keren, W. Graf, M. Angelo, D. Van Valen, Whole-cell segmentation of tissue images with human-level performance using large-scale data annotation and deep learning. *Nat Biotechnol* **40**, 555–565 (2022).

60. V. D. Blondel, J.-L. Guillaume, R. Lambiotte, E. Lefebvre, Fast unfolding of communities in large networks. *J. Stat. Mech.* **2008**, P10008 (2008).

61. T. Stylianopoulos, J. D. Martin, V. P. Chauhan, S. R. Jain, B. Diop-Frimpong, N. Bardeesy, B. L. Smith, C. R. Ferrone, F. J. Hornicek, Y. Boucher, L. L. Munn, R. K. Jain, Causes, consequences, and remedies for growth-induced solid stress in murine and human tumors. *Proceedings of the National Academy of Sciences* **109**, 15101–15108 (2012).

62. Y. L. Han, A. F. Pegoraro, H. Li, K. Li, Y. Yuan, G. Xu, Z. Gu, J. Sun, Y. Hao, S. K. Gupta, Y. Li, W. Tang, H. Kang, L. Teng, J. J. Fredberg, M. Guo, Cell swelling, softening and invasion in a three-dimensional breast cancer model. *Nat. Phys.* **16**, 101–108 (2020).

63. X. Zhang, X. Shi, D. Zhang, X. Gong, Z. Wen, I. Demandel, J. Zhang, A. Rossello-Martinez, T. J. Chan, M. Mak, Compression drives diverse transcriptomic and phenotypic adaptations in melanoma. *Proceedings of the National Academy of Sciences* **120**, e2220062120 (2023).

64. R. Kalluri, The biology and function of fibroblasts in cancer. *Nat Rev Cancer* **16**, 582–598 (2016).

65. E. Sahai, I. Astsaturov, E. Cukierman, D. G. DeNardo, M. Egeblad, R. M. Evans, D. Fearon, F. R. Greten, S. R. Hingorani, T. Hunter, R. O. Hynes, R. K. Jain, T. Janowitz, C. Jorgensen, A. C. Kimmelman, M. G. Kolonin, R. G. Maki, R. S. Powers, E. Puré, D. C. Ramirez, R. Scherz-Shouval, M. H. Sherman, S. Stewart, T. D. Tlsty, D. A. Tuveson, F. M. Watt, V. Weaver, A. T. Weeraratna, Z. Werb, A framework for advancing our understanding of cancer-associated fibroblasts. *Nat Rev Cancer*, 1–13 (2020).

66. G. Caligiuri, D. A. Tuveson, Activated fibroblasts in cancer: Perspectives and challenges. *Cancer Cell* **41**, 434–449 (2023).

67. C. R. Merritt, G. T. Ong, S. E. Church, K. Barker, P. Danaher, G. Geiss, M. Hoang, J. Jung, Y. Liang, J. McKay-Fleisch, K. Nguyen, Z. Norgaard, K. Sorg, I. Sprague, C. Warren, S. Warren, P. J. Webster, Z. Zhou, D. R. Zollinger, D. L. Dunaway, G. B. Mills, J. M. Beechem, Multiplex digital spatial profiling of proteins and RNA in fixed tissue. *Nat Biotechnol* **38**, 586–599 (2020).

68. D. R. Zollinger, S. E. Lingle, K. Sorg, J. M. Beechem, C. R. Merritt, GeoMx™ RNA Assay: High Multiplex, Digital, Spatial Analysis of RNA in FFPE Tissue. *Methods Mol Biol* **2148**, 331–345 (2020).

69. C. Gu, X. Shi, X. Dang, J. Chen, C. Chen, Y. Chen, X. Pan, T. Huang, Identification of Common Genes and Pathways in Eight Fibrosis Diseases. *Front. Genet.* **11**, 627396 (2021).

70. C. Xu, G. Tian, C. Jiang, H. Xue, M. Kuerbanjiang, L. Sun, L. Gu, H. Zhou, Y. Liu, Z. Zhang, Q. Xu, NPTX2 promotes colorectal cancer growth and liver metastasis by the activation of the canonical Wnt/β-catenin pathway via FZD6. *Cell Death Dis* **10**, 217 (2019).

71. J. Guinney, R. Dienstmann, X. Wang, A. de Reyniès, A. Schlicker, C. Soneson, L. Marisa, P. Roepman, G. Nyamundanda, P. Angelino, B. M. Bot, J. S. Morris, I. M. Simon, S. Gerster, E. Fessler, F. De Sousa E Melo, E. Missiaglia, H. Ramay, D. Barras, K. Homicsko, D. Maru, G. C. Manyam, B. Broom, V. Boige, B. Perez-Villamil, T. Laderas, R. Salazar, J. W. Gray, D. Hanahan, J. Tabernero, R. Bernards, S. H. Friend, P. Laurent-Puig, J. P. Medema, A. Sadanandam, L. Wessels, M. Delorenzi, S. Kopetz, L. Vermeulen, S. Tejpar, The consensus molecular subtypes of colorectal cancer. *Nat Med* **21**, 1350–1356 (2015).

72. I. Joanito, P. Wirapati, N. Zhao, Z. Nawaz, G. Yeo, F. Lee, C. L. P. Eng, D. C. Macalinao, M. Kahraman, H. Srinivasan, V. Lakshmanan, S. Verbandt, P. Tsantoulis, N. Gunn, P. N. Venkatesh, Z. W. Poh, R. Nahar, H. L. J. Oh, J. M. Loo, S. Chia, L. F. Cheow, E. Cheruba, M. T. Wong, L. Kua, C. Chua, A. Nguyen, J. Golovan, A. Gan, W.-J. Lim, Y. A. Guo, C. K. Yap, B. Tay, Y. Hong, D. Q. Chong, A.-Y. Chok, W.-Y. Park, S. Han, M. H. Chang, I. Seow-En, C. Fu, R. Mathew, E.-L. Toh, L. Z. Hong, A. J. Skanderup, R. DasGupta, C.-A. J. Ong, K. H. Lim, E. K. W. Tan, S.-L. Koo, W. Q. Leow, S. Tejpar, S. Prabhakar, I. B. Tan, Single-cell and bulk transcriptome sequencing identifies two epithelial tumor cell states and refines the consensus molecular classification of colorectal cancer. *Nat Genet* **54**, 963–975 (2022).

73. S. He, P. Lei, W. Kang, P. Cheung, T. Xu, M. Mana, C. Y. Park, H. Wang, S. Imada, J. O. Russell, J. Wang, R. Wang, Z. Zhou, K. Chetal, E. Stas, V. Mohad, P. Bruun-Rasmussen, R. I. Sadreyev, R. A. Hodin, Y. Zhang, D. T. Breault, F. D. Camargo, Ö. H. Yilmaz, J. J. Fredberg, N. Saeidi, Stiffness Restricts the Stemness of the Intestinal Stem Cells and Skews Their Differentiation Toward Goblet Cells. *Gastroenterology* **164**, 1137-1151.e15 (2023).

74. J. Cai, N. Zhang, Y. Zheng, R. F. de Wilde, A. Maitra, D. Pan, The Hippo signaling pathway restricts the oncogenic potential of an intestinal regeneration program. *Genes Dev.* **24**, 2383–2388 (2010).

75. M. Cordenonsi, F. Zanconato, L. Azzolin, M. Forcato, A. Rosato, C. Frasson, M. Inui, M. Montagner, A. R. Parenti, A. Poletti, M. G. Daidone, S. Dupont, G. Basso, S. Bicciato, S. Piccolo, The Hippo Transducer TAZ Confers Cancer Stem Cell-Related Traits on Breast Cancer Cells. *Cell* **147**, 759–772 (2011).

76. S. Piccolo, T. Panciera, P. Contessotto, M. Cordenonsi, YAP/TAZ as master regulators in cancer: modulation, function and therapeutic approaches. *Nat Cancer* **4**, 9–26 (2023).

77. R. J. Pelham, Y. Wang, Cell locomotion and focal adhesions are regulated by substrate flexibility. *PNAS* **94**, 13661–13665 (1997).

78. J. R. Tse, A. J. Engler, Preparation of Hydrogel Substrates with Tunable Mechanical Properties. *Current Protocols in Cell Biology* **47**, 10.16.1-10.16.16 (2010).

79. R. W. Tilghman, C. R. Cowan, J. D. Mih, Y. Koryakina, D. Gioeli, J. K. Slack-Davis, B. R. Blackman, D. J. Tschumperlin, J. T. Parsons, Matrix Rigidity Regulates Cancer Cell Growth and Cellular Phenotype. *PLOS ONE* **5**, e12905 (2010).

80. C. Pérez-González, G. Ceada, F. Greco, M. Matejčić, M. Gómez-González, N. Castro, A. Menendez, S. Kale, D. Krndija, A. G. Clark, V. R. Gannavarapu, A. Álvarez-Varela, P. Roca-Cusachs, E. Batlle, D. M. Vignjevic, M. Arroyo, X. Trepat, Mechanical compartmentalization of the intestinal organoid enables crypt folding and collective cell migration. *Nat Cell Biol* **23**, 745–757 (2021).

81. S. Conti, V. Venturini, A. Cañellas-Socias, C. Cortina, J. F. Abenza, C. Stephan-Otto Attolini, E. Middendorp Guerra, C. K. Xu, J. H. Li, L. Rossetti, G. Stassi, P. Roca-Cusachs, A. Diz-Muñoz, V. Ruprecht, J. Guck, E. Batlle, A. Labernadie, X. Trepat, Membrane to cortex attachment determines different mechanical phenotypes in LGR5+ and LGR5- colorectal cancer cells. *Nat Commun* **15**, 3363 (2024).

82. K. L. VanDussen, J. M. Marinshaw, N. Shaikh, H. Miyoshi, C. Moon, P. I. Tarr, M. A. Ciorba, T. S. Stappenbeck, Development of an enhanced human gastrointestinal epithelial culture system to facilitate patient-based assays. *Gut* **64**, 911–920 (2015).

83. S. K. Sarvestani, S. Signs, B. Hu, Y. Yeu, H. Feng, Y. Ni, D. R. Hill, R. C. Fisher, S. Ferrandon, R. K. DeHaan, J. Stiene, M. Cruise, T. H. Hwang, X. Shen, J. R. Spence, E. H. Huang, Induced organoids derived from patients with ulcerative colitis recapitulate colitic reactivity. *Nat Commun* **12**, 262 (2021).

84. Y. Shen, X. Wang, J. Lu, M. Salfenmoser, N. M. Wirsik, N. Schleussner, A. Imle, A. Freire Valls, P. Radhakrishnan, J. Liang, G. Wang, T. Muley, M. Schneider, C. Ruiz de Almodovar, A. Diz-Muñoz, T. Schmidt, Reduction of Liver Metastasis Stiffness Improves Response to Bevacizumab in Metastatic Colorectal Cancer. *Cancer Cell* **37**, 800-817.e7 (2020).

85. E. Lorenc, L. Varinelli, M. Chighizola, S. Brich, F. Pisati, M. Guaglio, D. Baratti, M. Deraco, M. Gariboldi, A. Podestà, Correlation between biological and mechanical properties of extracellular matrix from colorectal peritoneal metastases in human tissues. *Sci Rep* **13**, 12175 (2023).

86. A. Rubiano, C. Galitz, C. S. Simmons, Mechanical Characterization by Mesoscale Indentation: Advantages and Pitfalls for Tissue and Scaffolds. *Tissue Engineering Part C: Methods* **25**, 619–629 (2019).

87. O. Chaudhuri, J. Cooper-White, P. A. Janmey, D. J. Mooney, V. B. Shenoy, Effects of extracellular matrix viscoelasticity on cellular behaviour. *Nature* **584**, 535–546 (2020).

88. A. Elosegui-Artola, The extracellular matrix viscoelasticity as a regulator of cell and tissue dynamics. *Current Opinion in Cell Biology* **72**, 10–18 (2021).

89. P. P. Provenzano, K. W. Eliceiri, J. M. Campbell, D. R. Inman, J. G. White, P. J. Keely, Collagen reorganization at the tumor-stromal interface facilitates local invasion. *BMC Medicine* **4** (2006).

90. S. Furuhashi, M. A. Bustos, S. Mizuno, S. Ryu, Y. Naeini, A. J. Bilchik, D. S. B. Hoon, Spatial profiling of cancer-associated fibroblasts of sporadic early onset colon cancer microenvironment. *npj Precis. Onc.* **7**, 1–19 (2023).

91. S.-N. Lin, A. Musso, J. Wang, P. K. Mukherjee, G. A. West, R. Mao, R. Lyu, J. Li, S. Zhao, M. Elias, Y. Haberman, L. A. Denson, S. Kugathasan, M.-H. Chen, D. Czarnecki, D. Dejanovic, H. T. Le, J. Chandra, J. Lipman, S. R. Steele, Q. T. Nguyen, C. Fiocchi, F. Rieder, Human intestinal myofibroblasts deposited collagen VI enhances adhesiveness for T cells – A novel mechanism for maintenance of intestinal inflammation. *Matrix Biology* **113**, 1–21 (2022).

92. T. P. Driscoll, B. D. Cosgrove, S.-J. Heo, Z. E. Shurden, R. L. Mauck, Cytoskeletal to Nuclear Strain Transfer Regulates YAP Signaling in Mesenchymal Stem Cells. *Biophysical Journal* **108**, 2783–2793 (2015).

93. A. Elosegui-Artola, I. Andreu, A. E. M. Beedle, A. Lezamiz, M. Uroz, A. J. Kosmalska, R. Oria, J. Z. Kechagia, P. Rico-Lastres, A.-L. Le Roux, C. M. Shanahan, X. Trepat, D. Navajas, S. Garcia-Manyes, P. Roca-Cusachs, Force Triggers YAP Nuclear Entry by Regulating Transport across Nuclear Pores. *Cell* **171**, 1397-1410.e14 (2017).

94. J. W. Harding, I. N. Sneddon, The elastic stresses produced by the indentation of the plane surface of a semi-infinite elastic solid by a rigid punch. *Mathematical Proceedings of the Cambridge Philosophical Society* **41**, 16–26 (1945).

95. C. T. McKee, J. A. Last, P. Russell, C. J. Murphy, Indentation Versus Tensile Measurements of Young's Modulus for Soft Biological Tissues. *Tissue Engineering Part B: Reviews* **17**, 155–164 (2011).

96. Y. C. Fung, K. Fronek, P. Patitucci, Pseudoelasticity of Arteries and the Choice of Its Mathematical Expression. *American Journal of Physiology - Heart and Circulatory Physiology* **237**, H620–H631 (1979).

97. G. A. Holzapfel, *Nonlinear Solid Mechanics: A Continuum Approach for Engineering* (Wiley, Chichester ; New York, 1st edition., 2000).

98. J. Ferruzzi, M. R. Bersi, S. Uman, H. Yanagisawa, J. D. Humphrey, Decreased Elastic Energy Storage, Not Increased Material Stiffness, Characterizes Central Artery Dysfunction in Fibulin-5 Deficiency Independent of Sex. *J Biomech Eng* **137**, 031007 (2015).

99. P. Berens, **CircStat** : A *MATLAB* Toolbox for Circular Statistics. *J. Stat. Soft.* **31** (2009).

100. Y. Benjamini, Y. Hochberg, Controlling the False Discovery Rate: A Practical and Powerful Approach to Multiple Testing. *Journal of the Royal Statistical Society. Series B (Methodological)* **57**, 289–300 (1995).

101. D. Wu, G. K. Smyth, Camera: a competitive gene set test accounting for inter-gene correlation. *Nucleic Acids Research* **40**, e133 (2012).

102. A. Subramanian, P. Tamayo, V. K. Mootha, S. Mukherjee, B. L. Ebert, M. A. Gillette, A. Paulovich, S. L. Pomeroy, T. R. Golub, E. S. Lander, J. P. Mesirov, Gene set enrichment analysis: A knowledge-based approach for interpreting genome-wide expression profiles. *Proceedings of the National Academy of Sciences* **102**, 15545–15550 (2005).

103. DeepCell Label: https://github.com/vanvalenlab/deepcell-label, vanvalenlab (2025); https://github.com/vanvalenlab/deepcell-label.

104. J. W. Hickey, Y. Tan, G. P. Nolan, Y. Goltsev, Strategies for Accurate Cell Type Identification in CODEX Multiplexed Imaging Data. *Front. Immunol.* **12** (2021).

105. J. W. Hickey, W. R. Becker, S. A. Nevins, A. Horning, A. E. Perez, C. Zhu, B. Zhu, B. Wei, R. Chiu, D. C. Chen, D. L. Cotter, E. D. Esplin, A. K. Weimer, C. Caraccio, V. Venkataraaman, C. M. Schürch, S. Black, M. Brbić, K. Cao, S. Chen, W. Zhang, E. Monte, N. R. Zhang, Z. Ma, J. Leskovec, Z. Zhang, S. Lin, T. Longacre, S. K. Plevritis, Y. Lin, G. P. Nolan, W. J. Greenleaf, M. Snyder, Organization of the human intestine at single-cell resolution. *Nature* **619**, 572–584 (2023).

106. S.-W. Kim, J. Roh, C.-S. Park, Immunohistochemistry for Pathologists: Protocols, Pitfalls, and Tips. *J Pathol Transl Med* **50**, 411–418 (2016).

107. P. Bankhead, M. B. Loughrey, J. A. Fernández, Y. Dombrowski, D. G. McArt, P. D. Dunne, S. McQuaid, R. T. Gray, L. J. Murray, H. G. Coleman, J. A. James, M. Salto-Tellez, P. W. Hamilton, QuPath: Open source software for digital pathology image analysis. *Sci Rep* **7**, 16878 (2017).

108. S. J. DeCamp, V. M. K. Tsuda, J. Ferruzzi, S. A. Koehler, J. T. Giblin, D. Roblyer, M. H. Zaman, S. T. Weiss, A. Kılıç, M. De Marzio, C. Y. Park, N. C. Ogassavara, J. A. Mitchel, J. P. Butler, J. J. Fredberg, Epithelial layer unjamming shifts energy metabolism toward glycolysis. *Scientific Reports* **10**, 18302 (2020).

109. D. P. Maruri, M. Miron-Mendoza, P. B. Kivanany, J. M. Hack, D. W. Schmidtke, W. M. Petroll, V. D. Varner, ECM Stiffness Controls the Activation and Contractility of Corneal Keratocytes in Response to TGF-β1. *Biophysical Journal* **119**, 1865–1877 (2020).

ACKNOWLEDGMENTS

We thank Elena Seymour and Reyan Ghanim for conducting preliminary experiments on polyacrylamide substrates and Nathaniel Roberts for assisting with cell morphology quantifications. We also thank Manal Ali for assistance with the collection of both fresh and fixed primary tissues, and Dr. Dan Zhao for initial in vitro experiments. We gratefully acknowledge Dr. Huocong Huang for helpful discussions and guidance on the bioinformatic analysis of spatial RNA sequencing.

Funding:

University of Texas at Dallas Office of Research and Innovation through the CoBRA program (JF, EHH).

University of Texas at Dallas, Bioengineering Department Startup funds (JF).

University of Texas at Dallas, Bioengineering Researcher Award (NCH).

University of Texas Southwestern, Department of Surgery Startup funds (EHH, MHB).

University of Texas Southwestern Early Onset Colorectal Cancer Initiative (Simmons Comprehensive Cancer Center) (EHH).

National Institutes of Health grant R01 CA234307 (EHH).

National Institutes of Health grant U01 CA214300 (EHH).

Burroughs-Wellcome Trust (MHB).

American Society of Colon and Rectal Surgeons Resident Research Initiation Grant (MHB).

The work reported in this publication was supported by the National Cancer Institute of the National Institutes of Health under award number P30 CA142543 (CML).

University of Texas Whole Brain Microscopy Facility RRID:SCR_017949, and Axioscan 7 Award number 1S10ODO032267-01 to Denise Ramirez (Core Director).

Author Contributions:

Conceptualization: JF, EHH

Methodology: JF, RCF, IR, ARJ, SR, VDV, CML

Investigation: NCH, MHB, VVN, AK-S, HA, AK, AF, GC, CZ, MY

Pathology: ZC

Visualization: JF, NCH, MHB, CZ, MY

Supervision: JF, EHH

Writing – original draft: NCH, MHB, JF, EHH

Writing – review & editing: JF, EHH

Competing interests: Authors declare that they have no competing interests.

Data and materials availability: All data in the main text or in the supplementary materials are available upon request. Data and codes supporting the findings of this study are available from the corresponding authors upon reasonable request. Primary human tissues have been used throughout this manuscript and only histological blocks are available via deidentified Material Transfer Agreement (MTA). The GeoMx bulk transcriptome data on the human colon cancer and matched normal tissues, with PanCK, Vimentin, and CD45 stained and retrieved clusters have been deposited into the Gene Expression Omnibus and are available via GSE281413.

Supplementary Materials: Supplementary figures and discussions accompany this manuscript.

FIGURES

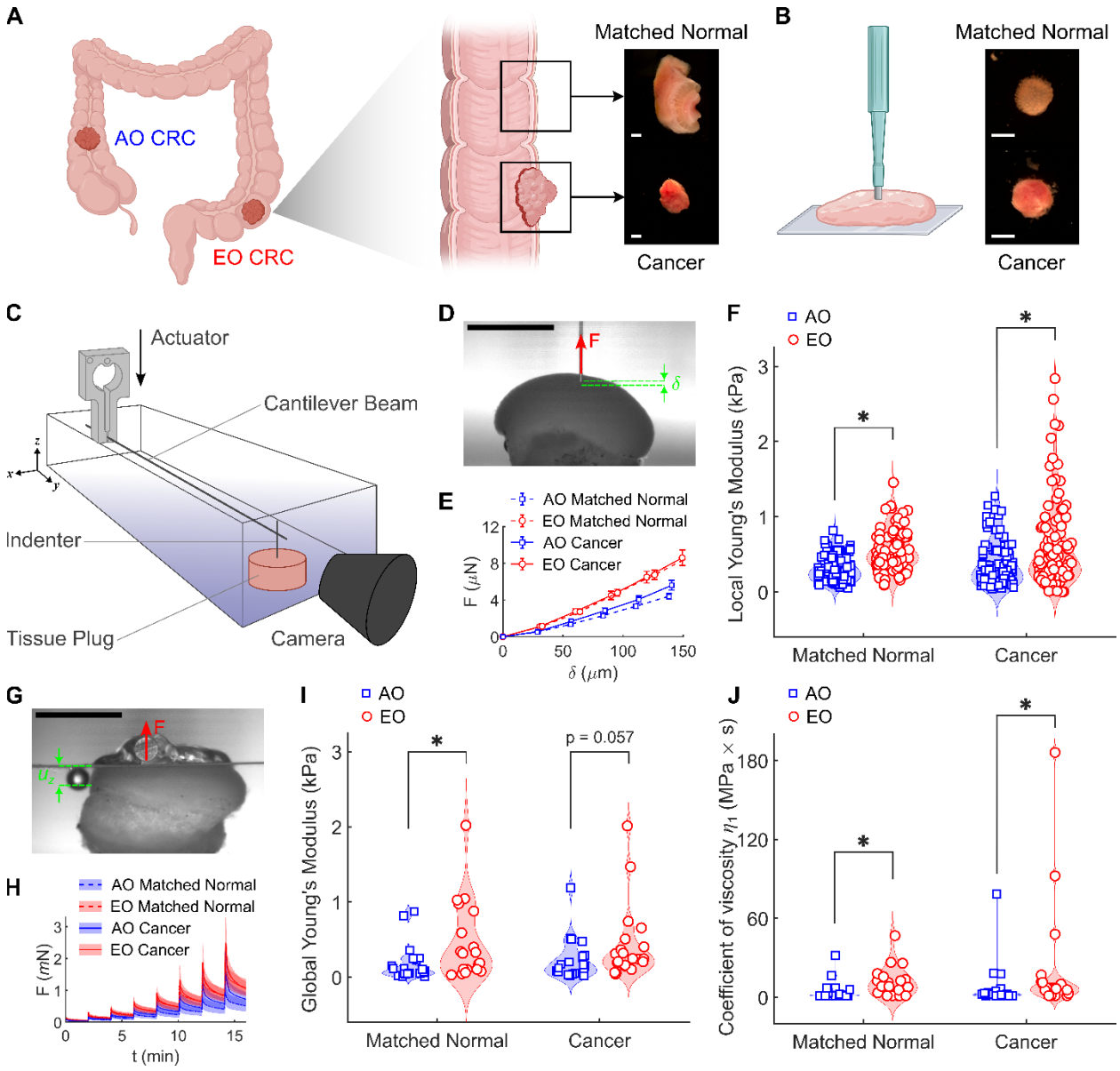

Figure 1. Primary tissues from sporadic early-onset colorectal cancer (EO CRC) patients exhibit increased material stiffness and viscosity across length scales. (**A**) Cancer and matched normal tissues were harvested from average onset (AO) and early onset (EO) colorectal cancer (CRC) patients undergoing surgical resection and (**B**) cylindrical specimens for mechanical characterization were prepared using a 3 mm biopsy punch. Scale bars, 2 mm. (**C**) Schematic of the mechanical testing setup, in which a cantilever beam of known stiffness was equipped with an

indenter for local (mesoscale) testing or with a flat platen for global (macroscale) testing. (**D**) Representative camera caption showing the imposed indentation (δ) and the resulting force (F) measured locally from a colorectal tissue specimen. Scale bar, 2 mm. (**E**) Average force-indentation curves and (**F**) associated stiffness values (quantified as local Young's moduli) measured for the four groups (n = 94 for AO Matched Normal, n = 89 for AO Cancer, n = 80 for EO Matched Normal, n = 102 for EO Cancer). (**G**) Representative camera caption showing the imposed displacement (u_z) and the resulting force (F) measured globally from a colorectal tissue specimen. Scale bar, 2 mm. (**H**) Average force evolution over time upon 8 consecutive stress relaxation steps and (**I**) associated stiffness values (quantified as global Young's moduli) and (**J**) fast coefficient of viscosity measured for the four groups (n = 21 for AO Matched Normal, n = 21 for AO Cancer, n = 19 for EO Matched Normal, n = 21 for EO Cancer). Mechanical data are presented as mean ± SEM while associated quantifications of stiffness and viscosity are presented as violin plots with data points indicating individual measurements. Statistical significance was assessed using a Scheirer-Ray-Hare test with Dunn's post-hoc test and Bonferroni correction. * indicates significant differences ($p < 0.05$) between cancer and matched normal tissues within onset groups (AO, EO) and between onset groups within tissue types (matched normal, cancer).

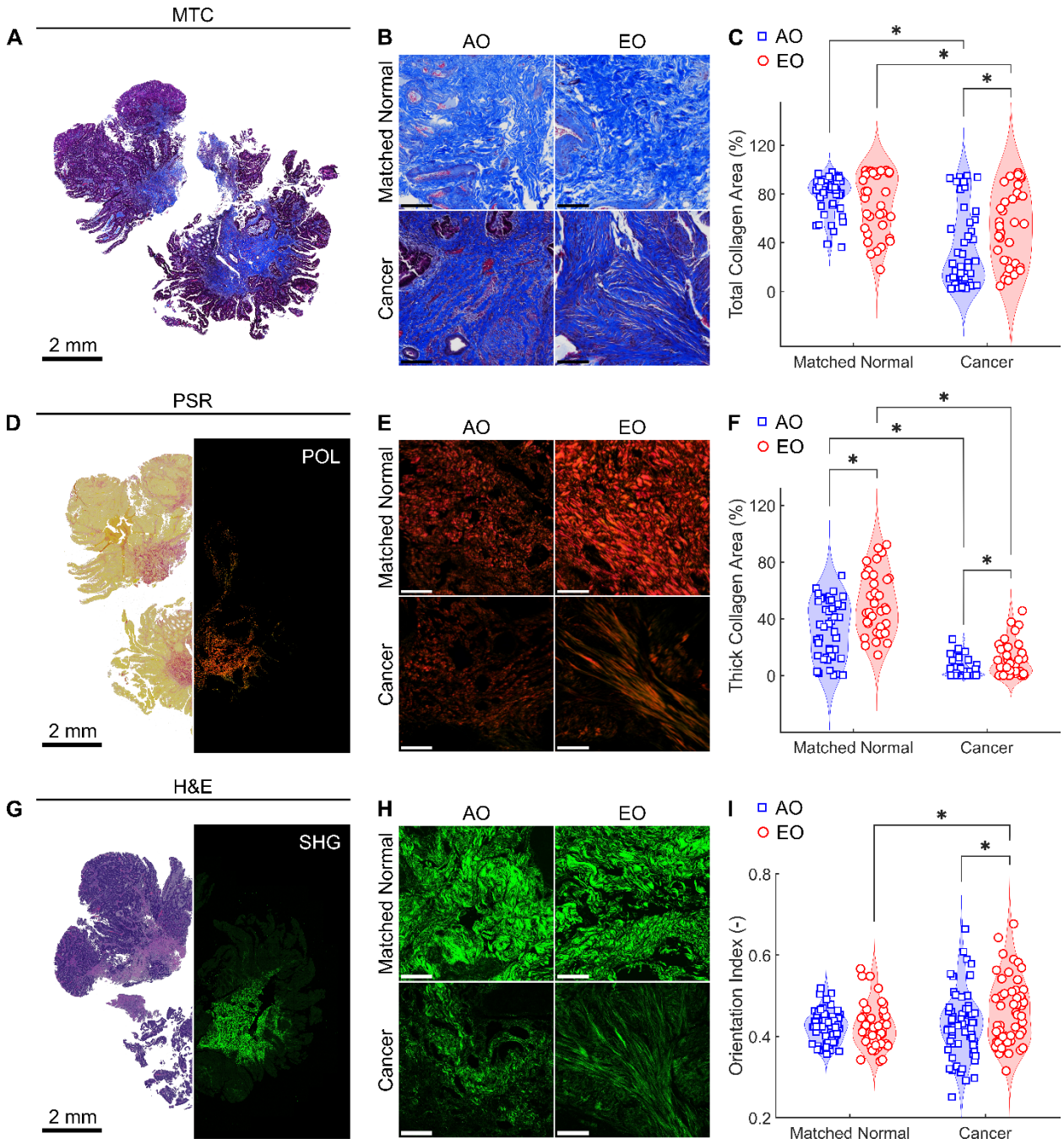

Figure 2. Tissues from sporadic EO CRC patients exhibit collagen remodeling consistent with fibrosis. (**A**) Masson's Trichrome (MTC) staining of a patient tissue sample and (**B**) representative zoomed-in images (1 mm × 1 mm) for the four groups. (**C**) Quantitative assessment of the area fraction occupied by collagen in the normal submucosa and in the tumor stroma (n = 45 for AO Matched Normal, n = 45 for AO Cancer, n = 35 for EO Matched Normal, n = 35 for

EO Cancer). (**D**) Picrosirius Red (PSR) staining of a patient tissue sample imaged under brightfield illumination (left) and under polarized light (POL, right) and (**E**) representative zoomed-in images (1 mm × 1 mm) for the four groups. (**F**) Quantitative assessment of the area fraction occupied by thick collagen fibers (red) in the normal submucosa and in the cancer stroma (n = 45 for AO Matched Normal, n = 45 for AO Cancer, n = 35 for EO Matched Normal, n = 35 for EO Cancer). (**G**) Hematoxylin and Eosin (H&E) staining of a patient tissue sample imaged under brightfield illumination (left) and using multiphoton Second Harmonic Generation (SHG, right) imaging, with (**H**) representative zoomed-in images (1 mm × 1 mm) for the four groups. (**I**) Quantitative assessment of collagen fiber alignment via a dimensionless orientation index in the normal submucosa and in the cancer stroma (n = 65 for AO Matched Normal, n = 64 for AO Cancer, n = 47 for EO Matched Normal, n = 55 for EO Cancer). Unless otherwise specified, scale bars indicate 200 μm. Data are presented as violin plots with data points indicating individual measurements. Statistical significance was assessed using a Scheirer-Ray-Hare test with Dunn's post-hoc test and Bonferroni correction. * indicates significant differences ($p < 0.05$) between cancer and matched normal tissues within onset groups (AO, EO) and between onset groups within tissue types (matched normal, cancer).

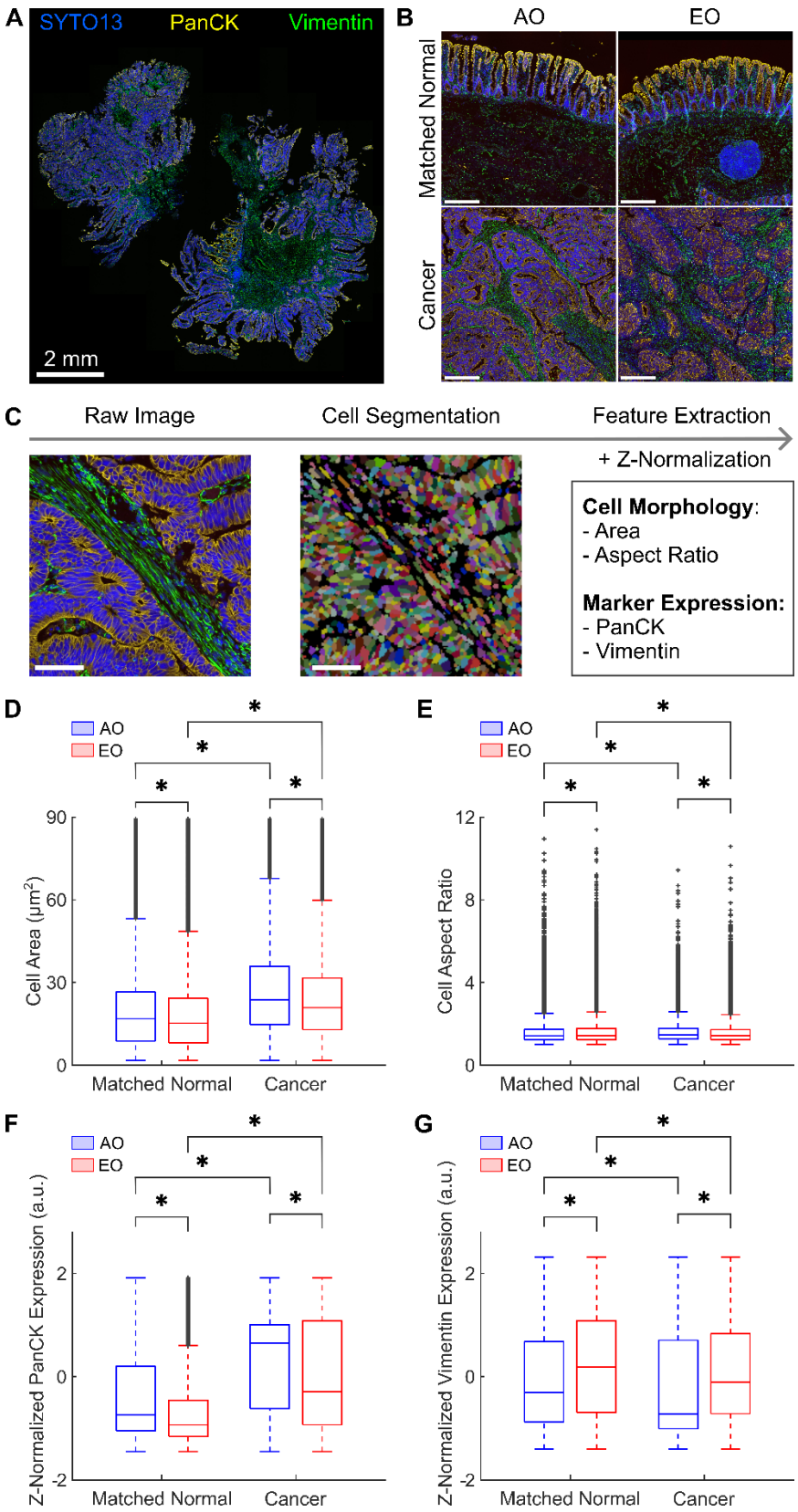
A
SYTO13
PanCK
Vimentin
2 mm
B
AO
EO
Matched Normal
Cancer
C
Raw Image
Cell Segmentation
Feature Extraction
+ Z-Normalization
Cell Morphology:
- Area
- Aspect Ratio
Marker Expression:
- PanCK
- Vimentin
D
AO
EO
Cell Area (μm²)
Matched Normal
Cancer
E
Cell Aspect Ratio
F
Z-Normalized PanCK Expression (a.u.)
G
Z-Normalized Vimentin Expression (a.u.)

Figure 3. Tissues from EO CRC patients reveal distinct epithelial and mesenchymal cellular phenotypes. (**A**) Immunofluorescence staining of a patient tissue sample and (**B**) representative zoomed-in images (1 mm × 1 mm) for the four groups. Pseudocoloring shows the SYTO13 nuclear marker in blue, the epithelial marker PanCK in yellow, and the stromal marker Vimentin in green. Scale bars, 200 µm. (**C**) Image analysis pipeline for immunofluorescence images includes cell segmentation and extraction of single-cell features. Scale bars, 50 µm. Box plots for (**D**) cell area, (**E**) cell aspect ratio, (**F**) z-normalized PanCK expression, and (**G**) z-normalized Vimentin expression show differences in cell morphology and marker expression across the four groups. The expressions of epithelial and stromal markers were z-normalized to facilitate comparisons across a large dataset (n = 176,681 for AO Matched Normal, n = 753,993 for AO Cancer, n = 379,626 for EO Matched Normal, n = 844,746 for EO Cancer). Statistical significance was assessed using a Scheirer-Ray-Hare test with Dunn's post-hoc test and Bonferroni correction. * indicates significant differences ($p < 0.05$) between cancer and matched normal tissues within onset groups (AO, EO) and between onset groups within tissue types (matched normal, cancer).

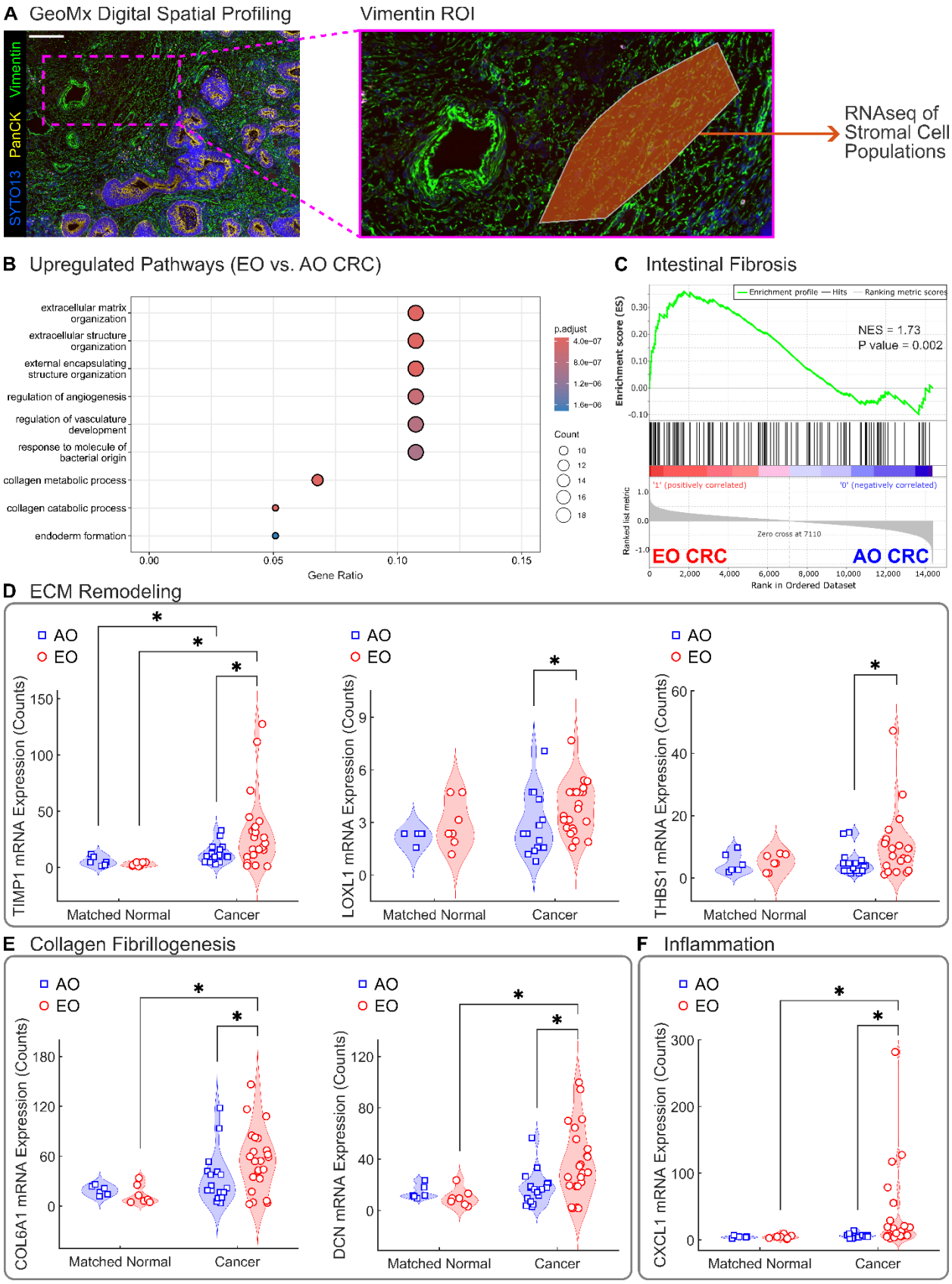
A GeoMx Digital Spatial Profiling
Vimentin ROI
Vimentin
PanCK
SYTO13
RNAseq of Stromal Cell Populations
B Upregulated Pathways (EO vs. AO CRC)
extracellular matrix organization
extracellular structure organization
external encapsulating structure organization
regulation of angiogenesis
regulation of vasculature development
response to molecule of bacterial origin
collagen metabolic process
collagen catabolic process
endoderm formation
Gene Ratio
p.adjust
Count
C Intestinal Fibrosis
Enrichment profile
Hits
Ranking metric scores
NES = 1.73
P value = 0.002
Enrichment score (ES)
'1' (positively correlated)
'0' (negatively correlated)
Ranked list metric
Zero cross at 7110
EO CRC
AO CRC
Rank in Ordered Dataset
D ECM Remodeling
AO
EO
TIMP1 mRNA Expression (Counts)
LOXL1 mRNA Expression (Counts)
THBS1 mRNA Expression (Counts)
Matched Normal
Cancer
E Collagen Fibrillogenesis
COL6A1 mRNA Expression (Counts)
DCN mRNA Expression (Counts)
F Inflammation
CXCL1 mRNA Expression (Counts)

Figure 4. Spatial transcriptomic profiling reveals pro-fibrotic signatures in the EO CRC stroma. (**A**) Immunofluorescence staining of a patient tissue sample and a representative vimentin-positive region of interest (ROI) used for digital spatial profiling with the GeoMx® RNA assay. Pseudocoloring shows the SYTO13 nuclear marker in blue, the epithelial marker PanCK in yellow, and the stromal marker Vimentin in green. Scale bar, 100 μm. (**B**) Gene ontology (GO) analysis showing the top upregulated pathways in EO CRC compared to AO CRC. The x-axis represents the Gene Ratio (number of genes in the pathway divided by the total number of genes analyzed), the bubble size is proportional to the count of genes in each pathway, and the color intensity indicates the adjusted p-value significance level. ECM and collagen remodeling are highlighted as key biological processes significantly enriched in the stroma of sporadic EO CRC. (**C**) Gene set enrichment analysis (GSEA) confirms upregulation of genes associated with intestinal fibrosis (*69*). Normalized enrichment score (NES = 1.73) and P value ($p = 0.002$) demonstrate significant upregulation of intestinal fibrosis in EO CRC. Expression levels of selected genes associated with (**D**) ECM remodeling (TIMP1, LOXL1, THBS1), (**E**) collagen fibrillogenesis (COL6A1, DCN), and (**F**) inflammation (CXCL1). Sample sizes indicate the number of ROIs analyzed for each group (n = 6 for AO Matched Normal, n = 7 for AO Cancer, n = 17 for EO Matched Normal, n = 23 for EO Cancer). Data are presented as violin plots with data points indicating individual ROIs. Statistical significance was assessed using a Scheirer-Ray-Hare test with Dunn's post-hoc test and Bonferroni correction. * indicates significant differences ($p < 0.05$) between cancer and matched normal tissues within onset groups (AO, EO) and between onset groups within tissue types (matched normal, cancer).

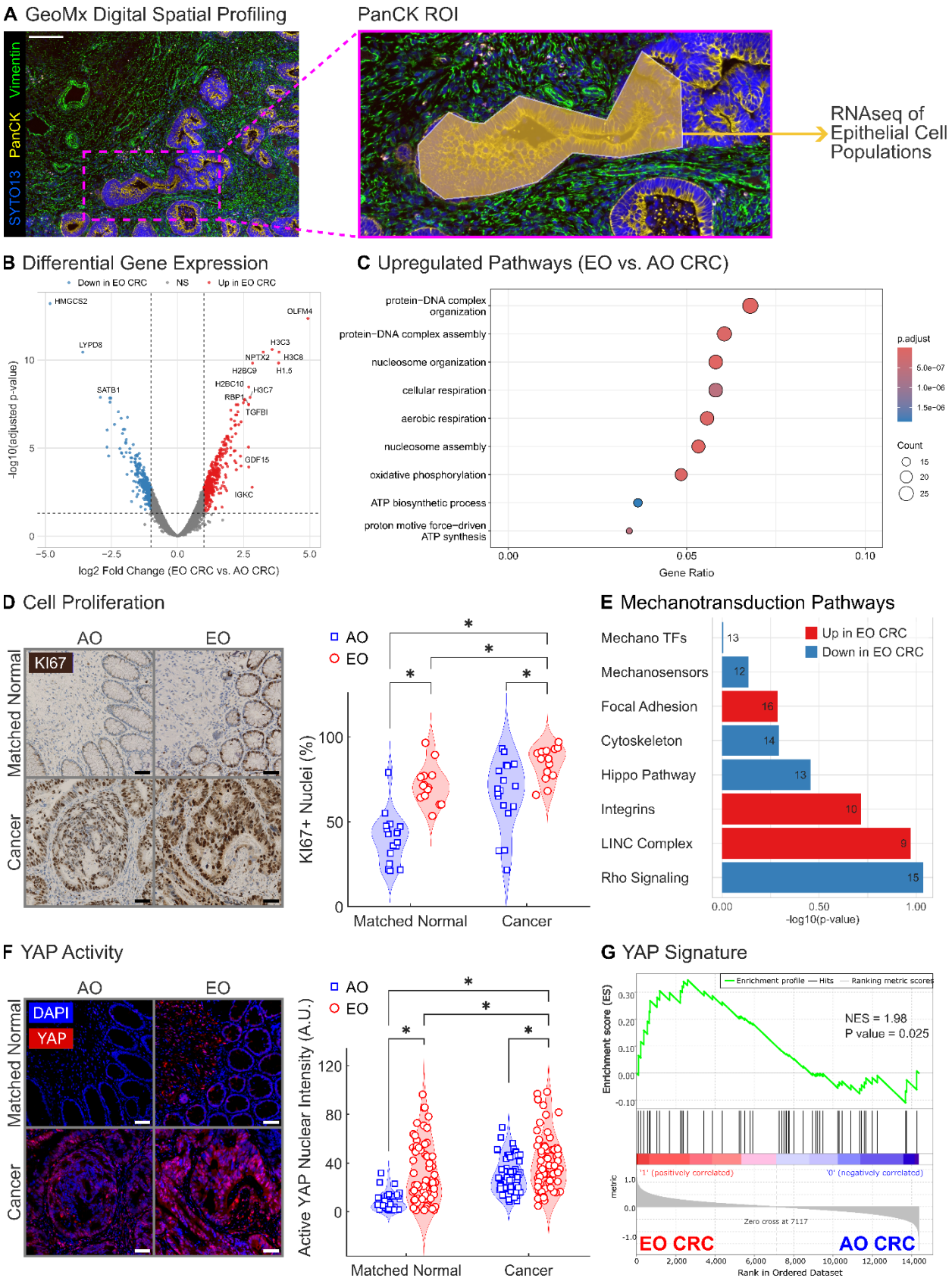
A GeoMx Digital Spatial Profiling
PanCK ROI
Vimentin
PanCK
SYTO13
RNAseq of Epithelial Cell Populations
B Differential Gene Expression
Down in EO CRC
NS
Up in EO CRC
HMGCS2
OLFM4
LYPD8
H3C3
NPTX2
H3C8
H2BC9
H1.5
H2BC10
H3C7
SATB1
RBP1
TGFBI
GDF15
IGKC
-log10(adjusted p-value)
log2 Fold Change (EO CRC vs. AO CRC)
C Upregulated Pathways (EO vs. AO CRC)
protein−DNA complex organization
protein−DNA complex assembly
nucleosome organization
cellular respiration
aerobic respiration
nucleosome assembly
oxidative phosphorylation
ATP biosynthetic process
proton motive force−driven ATP synthesis
Gene Ratio
p.adjust
Count
D Cell Proliferation
AO
EO
KI67
Matched Normal
Cancer
KI67+ Nuclei (%)
E Mechanotransduction Pathways
Mechano TFs
Mechanosensors
Focal Adhesion
Cytoskeleton
Hippo Pathway
Integrins
LINC Complex
Rho Signaling
Up in EO CRC
Down in EO CRC
-log10(p-value)
F YAP Activity
DAPI
YAP
Active YAP Nuclear Intensity (A.U.)
G YAP Signature
Enrichment profile
Hits
Ranking metric scores
NES = 1.98
P value = 0.025
Enrichment score (ES)
'1' (positively correlated)
'0' (negatively correlated)
Zero cross at 7117
EO CRC
AO CRC
Rank in Ordered Dataset

Figure 5. EO CRC epithelial cells exhibit enhanced proliferation and altered mechano-sensing. (**A**) Immunofluorescence staining of a tissue sample and a representative PanCK-positive region of interest (ROI) used for digital spatial profiling with the GeoMx® RNA assay. Pseudocoloring shows the SYTO13 nuclear marker in blue, the epithelial marker PanCK in yellow, and the stromal marker Vimentin in green. Scale bar, 100 μm. (**B**) Volcano plot highlights differential gene expression in PanCK-positive epithelial cells between EO and AO CRC. The x-axis represents log2 fold change (EO CRC vs AO CRC), and the y-axis shows the -log10 of adjusted p-values. Red dots indicate genes significantly upregulated in EO CRC (log2 fold change > 1, adjusted p-value < 0.05), blue dots indicate genes significantly downregulated in EO CRC (log2 fold change < -1, adjusted p-value < 0.05), and grey dots represent non-significantly differentially expressed genes. (**C**) Gene ontology (GO) analysis showing the top upregulated pathways in EO CRC compared to AO CRC. (**D**) Ki67 immunohistochemistry staining of tissue samples confirmed increased cell proliferation in epithelial cells from EO CRC. (**E**) Mechanotransduction pathway enrichment analysis in epithelial cells comparing EO vs. AO CRC. Bar plot shows the significance (-log10 p-value) of eight distinct mechanotransduction-related gene sets. Bars are colored according to pathway direction (red = upregulated in EO CRC, blue = downregulated in EO CRC), and numbers at the end of each bar indicate the number of genes in each pathway detected in our data. (**F**) YAP immunofluorescence demonstrates elevated active nuclear YAP in epithelial cells form EO CRC patient tissues. Staining of matched normal and cancer tissue samples using active (non-phosphorylated) YAP was followed by quantification of nuclear intensity for active YAP. (**G**) Gene set enrichment analysis (GSEA) confirms upregulation of an established YAP signature (*75*). Normalized enrichment score (NES = 1.98) and P value (p = 0.025) demonstrate significant upregulation of YAP activity in EO CRC. Data are presented as

violin plots with data points indicating individual ROIs. Statistical significance was assessed using a Scheirer-Ray-Hare test with Dunn's post-hoc test and Bonferroni correction. * indicates significant differences ($p < 0.05$) between cancer and matched normal tissues within onset groups (AO, EO) and between onset groups within tissue types (matched normal, cancer).

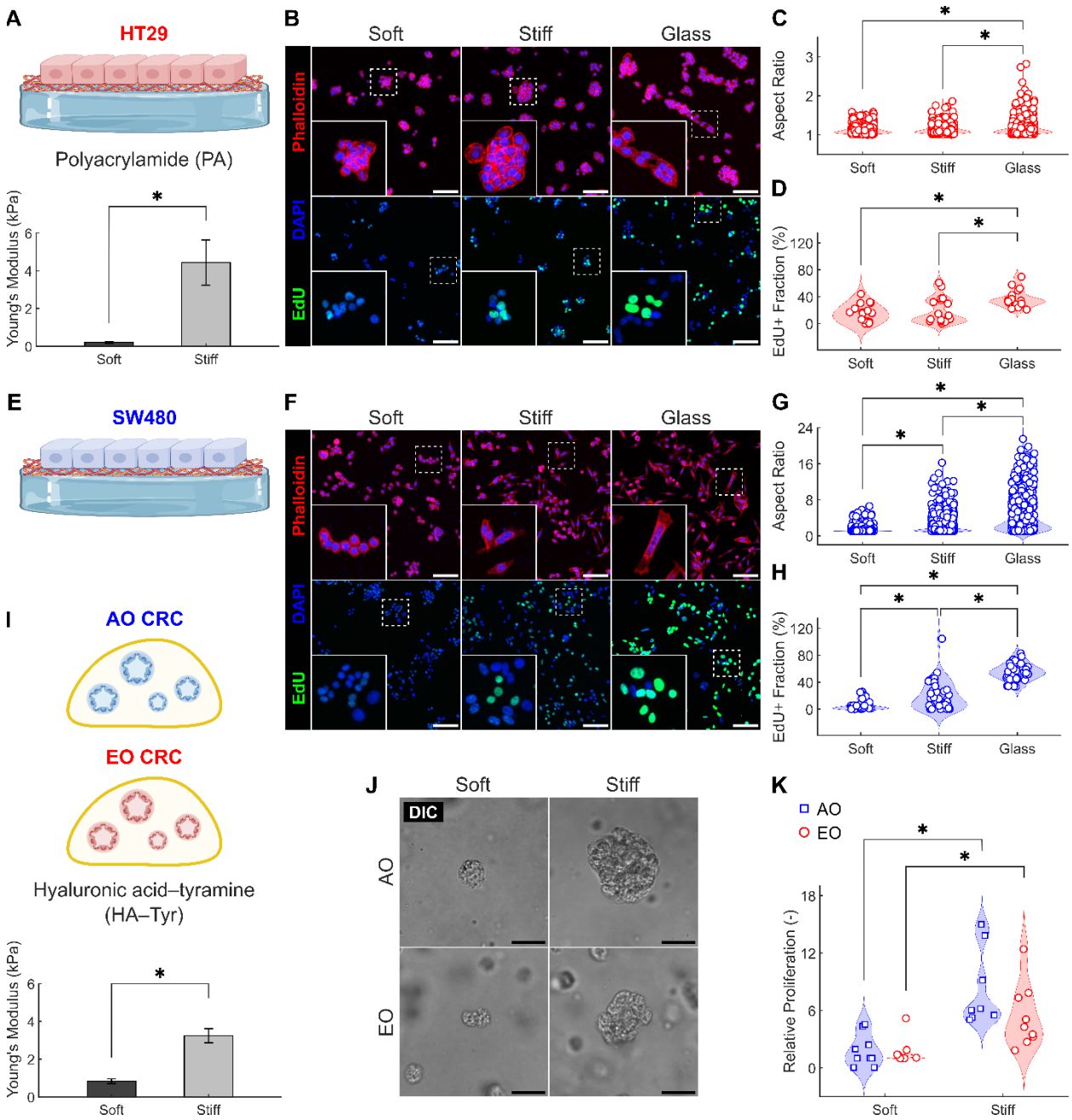

Figure 6. Microenvironmental stiffness alters epithelial morphology and proliferation in CRC cell lines and in patient-derived organoids. (**A**) Schematic representation of HT29 cells (44-year-old female) cultured on 2D polyacrylamide (PA) substrates of graded stiffness coated with Matrigel to investigate mechanobiological regulation of CRC cells. We reproduced the mechanical properties of colorectal tissues by employing soft PA gels ($E = 0.2 \pm 0.05$ kPa, n = 10)

and stiff PA gels (E = 4.4 ± 1.2 kPa, n = 9). (**B**) Immunofluorescence staining using phalloidin (red), DAPI (blue), and EdU (green) on cells cultured on graded substrate stiffness for 72 hours. Glass was used as a positive control of nearly infinite stiffness. Scale bars, 100 μm. (**C**) Aspect ratio of HT29 cells (n = 543 for soft PA, n = 631 for stiff PA, and n = 736 for glass) was quantified using 6 biological replicates and 6 ROIs per replicate, with 5-to-31 cells measured per ROI. (**D**) EdU incorporation in HT29 cells (n = 18 for soft PA, n = 18 for stiff PA, and n = 18 for glass) was quantified using 3 biological replicates and 6 ROIs per replicate. (**E**) Schematic representation of SW480 cells (50-year-old male) cultured on 2D PA substrates of graded stiffness coated with Matrigel. (**F**) Immunofluorescence staining of SW480 cells cultured on graded substrate stiffness for 72 hours. Scale bars, 100 μm. (**G**) Aspect ratio of SW480 cells (n = 771 for soft PA, n = 769 for stiff PA, and n = 659 for glass) was quantified using 6 biological replicates and 6 ROIs per replicate, with 15-to-52 cells measured per ROI. (**H**) EdU incorporation in SW480 cells (n = 30 for soft PA, n = 36 for stiff PA, and n = 36 for glass) was quantified using 5-to-6 biological replicates and 6 ROIs per replicate. (**I**) Schematic representation of 3D organoids derived from AO and EO CRC patients cultured in hyaluronic acid-tyramine (HA-Tyr) hydrogels with tunable stiffness. We reproduced the mechanical properties of colorectal tissues by employing soft HA-Tyr gels (E = 0.8 ± 0.1 kPa, n = 7) and stiff HA-Tyr gels (E = 3.2 ± 0.4 kPa, n = 7). (**J**) Representative DIC images of patient-derived organoids from AO and EO CRC patients cultured in soft and stiff HA-Tyr hydrogels for 7 days. Scale bars, 20 μm. (**K**) Quantification of normalized organoid viability in soft and stiff hydrogels using CellTiter-Glo® 3D assay shows that viability increases with stiffness. For each group (AO CRC and EO CRC), we utilized 3 biological replicates (patient donors) and 3 technical replicates (3 organoid-seeded hydrogels) per group, resulting in a total of n = 9 samples per group. Mechanical data are presented as mean ± SEM. Cell

morphology, proliferation, and viability data are presented as violin plots with data points indicating individual measurements. * indicates statistically significant differences ($p < 0.05$) between groups. Statistical significance was assessed using Scheirer-Ray-Hare test followed by Dunn's post-hoc test with Bonferroni correction. * indicates significant differences ($p < 0.05$) in pairwise stiffness comparisons within each substrate type.

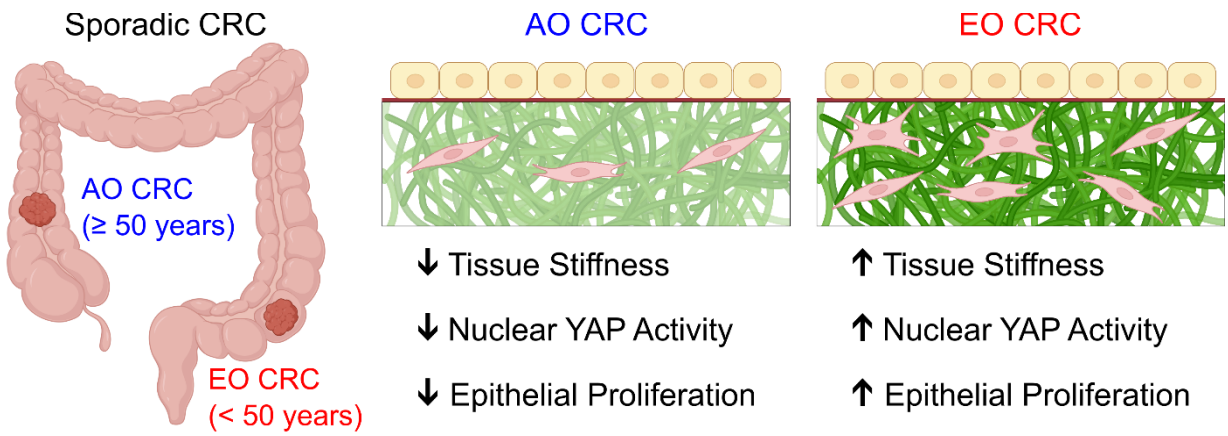

Figure 7. Summary of biomechanical and mechanobiological hallmarks of EO CRC. Using primary patient samples, our study quantified biomechanical, histological, transcriptional, and phenotypic differences between AO CRC and EO CRC. We find that EO CRC is associated with changes in collagen organization due to the activity of stromal cells, which results in increased tissue stiffness as measured via meso-scale indentation and macro-scale compression. These changes in connective tissue mechanics result in increased nuclear activity of YAP and increased epithelial proliferation.